ATV control

regulating a 4WD/4WS autonomous guided vehicle

Boot, J.

Award date:
2005

ATV Control

regulating a 4WD/4WS autonomous guided vehicle

Johan Boot

DCT Report no: 2005.31
2004-2005

TU/e Master's Thesis
2004-2005

Supervisors and committee members:
Prof. dr. ir. M. Steinbuch (TU/e)
Ir. P.C. Teerhuis (TU/e)
Dr. S.K. Advani (ADSE)
Dr. ir. W.H.J.J. van Staveren (ADSE)
Dr. ir. I.J.M. Besselink (TU/e)

Eindhoven University of Technology
Department of Mechanical Engineering
Division Dynamical Systems Design
Control System Technology group

Aircraft Development and
Systems Engineering B.V.
ADSE
Hoofddorp

Abstract

A four wheel driven and four wheel steered maneuverable vehicle is currently subject of research at ADSE. Due to high demands in acceleration tracking a new controller incorporating tyre dynamics needs to be developed.

Main difficulties for control are the overactuation of the vehicle and non-linearity's, which are dependent of velocity and cornering. Current control allocation techniques for overactuated systems have difficulties to include actuator dynamics. Instead of distributing control action among the actuators, a new allocation technique is developed. Outputs that correspond with unfeasible actuator combinations are added to the system. The number of system outputs now equals the number of system inputs and standard $\mathcal{H}_2$ control is applied. Velocity dependent controller switching is used for different working points.

The newly developed control system attains a significantly faster response than possible with currently available solutions. Multibody simulations have proven that all requirements are fulfilled and that the tyre forces are distributed optimally.

Preface

This past year I have been working on my master's thesis. It started as a new challenge where still many possibilities were open. Clear was that I would work on the newly to be designed ATV at ADSE, but the specific subject was still undetermined. Because of the travel distance I started working partly at the university in Eindhoven and partly at ADSE in Hoofddorp.

After a period of working on several diverse subjects in the project team, the choice for the design of the vehicle controller was made. During the validation of a first controller, it turned out that an advanced controller had to be designed instead of focusing on a practical and experimental assignment. Both the first period of working in a team on practical subjects as the second period of mostly theoretical issues have proved to be an educational and pleasant time.

I want to thank all the people who have helped and supported me during this research. Professor Maarten Steinbuch for his overlook, Sunjoo Advani for creating the possibilities for this assignment and always being positive, Piet Teerhuis for his weekly guidance at university, Jan-Willem van Staveren for his in depth technological help, Gert-Jan Ransijn for involving me into everything concerning the project, Igo Besselink for participating in the committee, my roommates at university and all the colleagues at ADSE who are nice people to work with and good company during the Friday afternoon 'borrel'.

In my personal life I want to thank my family for their support. I can always count on them and they are a great family. Finally I want to thank my beloved girlfriend, Siân Hillier for her care, her supporting words and the grammatical corrections she suggested.

Johan Boot, March 2005

Contents

Introduction

Electric driven vehicles start playing an increasingly important role in modern life. Hybrid cars like the Toyota Prius acquire a considerable share on the market. The recently developed Phileas Bus [1] which is autonomously guided by magnets in the road is commuting between Eindhoven train station and the airport. In 2002, General Motors presented their concept vehicle AUTOnomy which is completely electric driven. Also, in the TNO Automotive laboratory in Veldhoven, the autonomously guided electric vehicle VEHIL [2] is being used for developing and testing intelligent vehicles.

In this trend, ADSE B.V. in Hoofddorp, the Netherlands, is investigating four wheel steered (4WS) and four wheel driven (4WD) electric vehicles. Such a vehicle on which every wheel can be driven and steered independently will be called ADSE Test Vehicle or ATV. The ATV will be the size of a small truck and can be used for extreme maneuverable driving and automatic guidance.

A control system for this vehicle must be designed. Whether the vehicle will be handled by a person or a tracking controller does not make a fundamental difference. The correspondence is that a reference velocity and acceleration need to be tracked accurately and quickly.

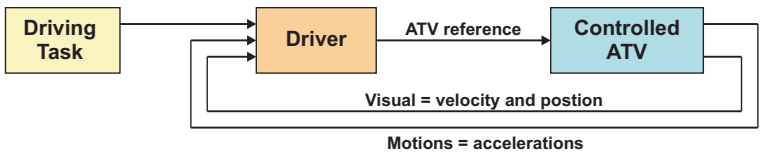

Figure 1: Scheme of driver and ATV in closed-loop

Fast tracking of velocities and accelerations will provide the driver and passengers a smooth ride. Secondly, if the driver or position controller is imag-

ined in closed-loop as depicted in figure 1, a small time delay of the controlled ATV is desired to make the system easy to control. For an autonomously guided vehicle, this means that a high bandwidth is possible. A human driver will need less control effort which does not exhaust the driver and offers a safe ride. Shorter response times than existing in current solutions are demanded for the ATV.

A main problem in controlling a vehicle like the ATV is the overactuation. Four wheels can be both driven and steered independently which totals eight inputs that can be manipulated. This, while only velocity/acceleration in three directions needs to be tracked. Traditional techniques use control allocation to solve this problem. Control effort is distributed among the different actuators. Actuators are assumed to react instantly and performance is lost in reality. By including forbidden control combination as additional system outputs, the static allocation in not necessary any more. A new strategy is developed which takes actuator dynamics into account. High performances and short response times can be obtained using this technique.

Chapter 1

Objectives and problem formulation

The objective of this report is to design a control system for the ADSE Test Vehicle or ATV. The control system has to drive and steer the ATV in such a way that the driver will feel the prescribed longitudinal, lateral and yaw acceleration according to reference while keeping the ATV close to its planned track. No tracking on position level is required in this thesis, however, the real position is only allowed to slowly stray away. This coincides with good tracking on velocity level. Most critical for driver perception and thus controller quality is the time delay between reference and real acceleration in the ATV center of gravity. This must stay below 40 ms for frequencies up to 2 Hz and gain errors should not be more than 5%. Since the ATV is an experimental vehicle for testing purposes, it operates at safe velocities varying between 15 and 40 km/h. Additional requirements are summarized in appendix A. It has to be determined if these requirements can be reached with the current configuration.

Difficulties will be found in the over-actuation of the platform. Every corner module has a steering motor and a driving motor. With four wheels this already comes down to eight actuators while there are only three degrees of freedom to be controlled. Not every input combination is feasible, when steering for example the front wheels towards each other, unnecessary high tyre forces and energy losses are generated. The allowable steering combinations position the wheels at different angles relative to the vehicle and makes the system non-linear. Imagine cornering over a small radius where the inner wheel is steering under an enlarged angle compared to the outer wheel. The slip-force characteristics of the tyres are also non-linear. In sit-

uations with large amounts of slip, more slip can even result in a lower tyre force. This is a nonlinear and unstable process, which is difficult to detect and control.

To reach the objectives while dealing with these difficulties, some sub-problems have to be solved.

- A literature survey in control of autonomously guided vehicles must be done. In the broader field of automotive control, a lot of research has been done. The found control solutions have to be tested on their results and compatibility with the ATV control goals.
- Good models of the system have to be found. These models have to represent the system behavior well, but not get too complicated in the sense they are unsuitable for control design.
- The most suitable control system has to be designed and evaluated. The overactuation and non-linearitys have to be taken into account during this design.

Chapter 2

System description

2.1 Dimensions

In this chapter, the ATV system will be defined and described. A number of concepts are designed and evaluated by ADSE [3]. By choosing the least complicated design, this report is attempting to keep focus on the most important issues. Further, it is not necessary that the used design exactly resembles one of the designs made by ADSE. During the modeling and control design, it will be taken into account that the models have to be suitable for other control designs with only minor changes. Assumptions made during modeling are summarized in appendix B.

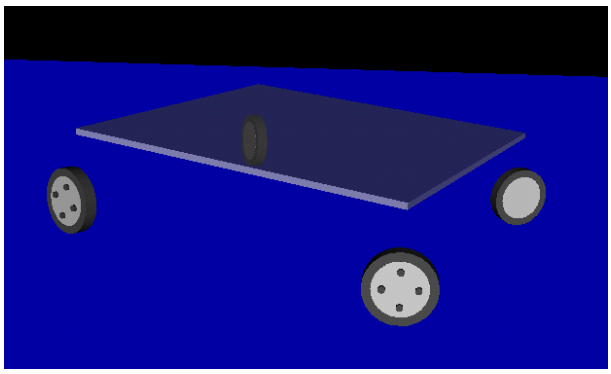

Figure 2.1: ATV model showed during multibody simulations

One of the original ATV designs is chosen to be used in this report. Existing reference material produced by ADSE can be used in this way. Through

transparant design, influences of other parameter variations will be shown. Figure 2.1 shows a 3-dimensional close up of the basic components of the ATV. The main platform and four corner modules including wheels, tyres and not shown, the suspension system. The individual components are assumed to be rigid.

The system which will be used from now on, has some small adaptations to the original design. The platform is driven by 4 wheel motors with a built-in planar reduction. The mass distribution is divided equally and the inertias in x and y direction are adapted such they are symmetric. The mass and inertia of the top mounts of the corner modules are included in the platform. The corner modules consist of only unsprung mass. Unsprung mass is the mass which is not suspended such as wheels and wheel carriers. The suspended platform is the sprung mass. A top view of the system is schematically depicted in figure 2.2.

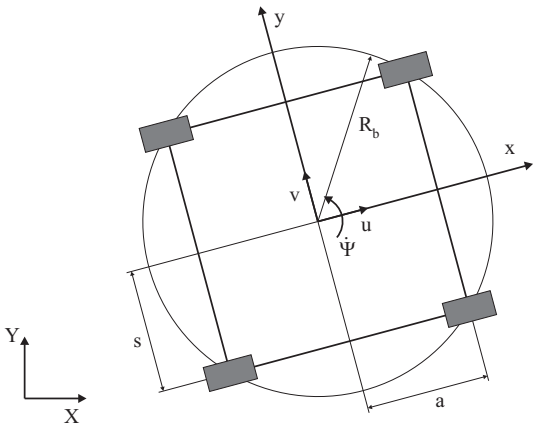

Figure 2.2: Top view of platform

Where X the global x-axis, Y the global y-axis, x the ATV-fixed x-axis, y the ATV-fixed y-axis, u the longitudinal velocity at the platform center of gravity (COG), v the lateral velocity at the platform COG, $\dot{\Psi}$ the rotational velocity, R_b the radius of the main body, a half the axle base and s half the track width.

Dimensions of the different parts are chosen as:
R_b= 4 [m]
a =$2\sqrt{2}$ [m]
s =$2\sqrt{2}$ [m]

Where the masses, inertias and heights of the centers of gravity are according to table 2.1.

Table 2.1: Mass and inertia

Element	Mass [kg]	I_{xx} $[kg/m^2]$	I_{yy} $[kg/m^2]$	I_{zz} $[kg/m^2]$	h [m]
Total	8000	40000	40000	65000	1.45
Platform	5600	19667	19667	26400	1.66
CM	600	100	100	50	0.95

To obtain these inertias, data of the complete system and the corner modules is used. The inertia and center of gravity of the platform with equipment has to apply to the next equations. First of all, the total center of gravity height is the weighed average of the independent center of gravity heights.

$$m_{total}h_{total} = m_{platform}h_{platform} + \sum_{i=1}^{4} m_{CM,i}h_{CM,i} \tag{2.1}$$

And the total inertia is determined with Steiner's formula. The total inertia is the sum of inertias plus the sum of the masses of the independent components multiplied with their squared distance r from the COG.

$$I_{total} = I_{platform} + m_{platform}r^2_{total-platform} + \sum_{i=1}^{4} I_{CM,i} + m_{CM,i}r^2_{total-CM,i} \tag{2.2}$$

2.2 Suspension

The actuators of the ATV generate forces in the horizontal plane at floor level. Because of an elevated center of gravity, also an undesired torque is produced, which generates pitch and roll effects. Other sources of undesired motions are an uneven road and tyre unroundness. All these parasitic movements have to be dampened. The tyres are not suitable for energy dissipation since they mainly behave as springs. A suspension system with dampers will be used to dissipate this energy and damp the parasitic movements.

For this damping task, the suspension system needs to be tuned. ADSE tuned the suspension system by simulation and manual trial and error optimization of the suspension stiffness and damping. An alternative approach is looked for to tune the suspension parameters in a structural way. This analysis is performed in appendix C. An optimal spring stiffness of 250,000 N/m and damping constant of 18,000 Ns/m are found.

The suspension system can also be used for other purposes. When a vehicle starts braking or cornering with a vertical suspension system, the car will start rotating around an axis on the road surface. This axis is called the roll axis and is defined by the roll poles of the front and rear suspension if there is no influence of the tyres assumed. By placing the vertical wheel travel under an angle, the roll poles of the vehicle can be changed. See references [4] and [5]. Anti-roll during cornering is now created. Most vehicles have different heights for the front roll pole and the rear roll pole, which creates a non horizontal roll axis. This is done to obtain good understeer/oversteer characteristics. In the ATV design, a symmetric design is chosen. The vehicle will be all wheel steered and driven which does not give the demand of certain understeer/oversteer characteristics. Also, a symmetric design in longitudinal and lateral direction is chosen to obtain the same properties for roll and pitch, which are both important for the ATV. During suspension deflections, the roll center generally will move. In this analysis this position is assumed constant.

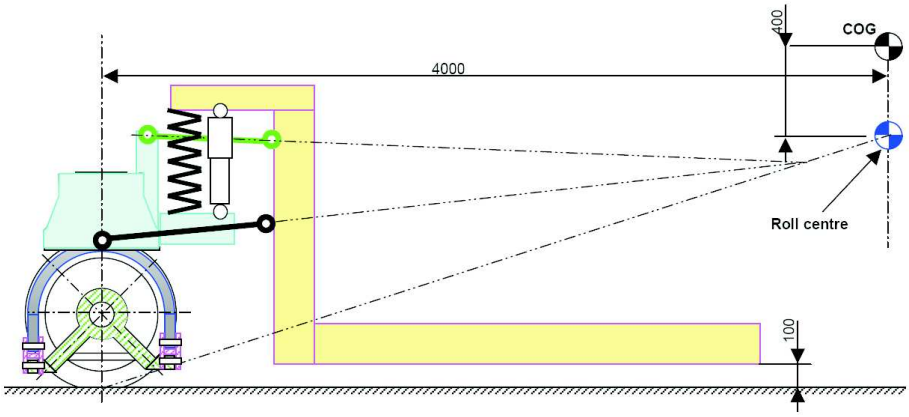

Figure 2.3: Scheme of ATV double wishbone suspension with roll-pole

The position of the roll center is determined by the angle between the vertical axis and the line under which the wheel will translate when the wheel moves up or down. The line, originating in the tyre contact point and perpendicular to this translation is drawn as the lowest dotted line in figure 2.3. The roll pole is determined by the point where this line crosses the same line from the wheel placed on the other side of the vehicle. In the case of a vertical suspension system, the perpendicular will be horizontal at road level, which coincides with a roll center at ground level. The height of the roll pole of the ATV is constructed 400 mm below the center of gravity of the ATV platform.

2.3 Tyres

In the current configuration, the platform is supported by four tyres. With the mass of about 8000 kg, a nominal vertical load of about 19,620 N per tyre is present. During longitudinal or lateral accelerations, dynamical loads can increase up to almost twice this amount. A truck tyre is chosen to withstand these high loads. The identification code of this tyre is 315-80-R22. The first number represents the section width [mm]. The second for the aspect ratio between section height and section width [%]. The R stands for the radial tyre construction and the last number for the rim diameter in inches. The outer diameter equals the rim diameter with twice the section height added.

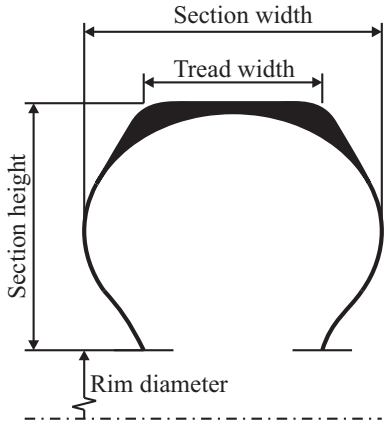

Figure 2.4: Tyre dimensions

$$Outer\ diameter = 22 \cdot 25.4 + 2 \cdot 315 \cdot 0.80 = 1062.8\ [mm] \tag{2.3}$$

This truck tyre is chosen because of its ability to resist the demanded loads and the availability of a measurement based model of this tyre. A specific choice of the tyre can be done in a later stage. It is more important that this research provides insight in making a founded decision concerning which tyres should be used.

The source for the used tyre properties is the file `Truck_315_80R22.tir`. This file contains the tyre parameters belonging to the magic formula tyre model as will be discussed in reference [15] and appendix F. The tyre parameters are determined by real measurements and the model is suitable for use in Matlab/Simulink. Both the tyre parameters as the model are commercially available at TNO [6]. The most important parameters are summarized in table 2.2.

Table 2.2: Tyre parameters

Variable	Unit	Description
C_{fz}	$1.0 \cdot 10^6$ $[N/m]$	Vertical carcass stiffness
D_{fz}	500 $[Ns/m]$	Vertical damping
C_{fx}	$996,530$ $[N/m]$	Longitudinal carcass stiffness
C_{fy}	$525,180$ $[N/m]$	Lateral carcass stiffness
$C_{f\kappa}$	$265,020$ $[Ns/m]$	Longitudinal slip stiffness at ATV average load
$C_{f\alpha}$	$148,230$ $[Ns/m]$	Vertical slip stiffness at ATV average load
μ_x	0.81 $[-]$	Longitudinal friction coefficient
μ_y	0.72 $[-]$	Lateral friction coefficient

Carcass stiffness is created by resistance of the walls of the tyres added with the effect of the compressed air. The longitudinal and lateral stiffness will differ. This is caused by the construction of the tyre. It can be imagined that the tyre carcass will give less resistance in lateral direction than in longitudinal direction where the tyre wall can resist the in-plane shear deformations better. A spring can be seen as the mechanical analogy of this tyre property.

The slip stiffness determines the amount of resistance to slip. This completely different tyre property is determined by contact patch and road interaction. Slip stiffness is analogous to a mechanical damper. Furthermore, the maximum amount of force produced by a tyre is limited. The ratio between maximum horizontal force and vertical force is called the friction coefficient. A more detailed explanation of tyre models can be found in appendix F.

2.4 Actuators and sensors

Actuators

For control design, the actuators and sensors of the system are defined. The number of actuators equals twice the number of corner modules, which makes the number of actuators eight in this case. Four actuators are the electro motors driving the wheels. The other four are the hydraulic cylinders steering the vehicle.

The electrical system of the motor can be modeled as a first order system

with a motor time constant τ_m of typically 0.0002 [s]. The motor time constant is so small, that the electric system will be approached by an instant reaction in this research. The inertia of the motor will have much more influence on the system dynamics. In this case, the planetary set is already taken into account for increasing motor torque and the motor inertia is added to the wheel. The maximum torque that can be produced depends on the maximum allowable current.

$$\mid T_{mi} \mid \leq 11,000\ Nm \tag{2.4}$$

The maximum speed is limited by the maximum voltage but will not exceed this limit without trespassing security constraints of the maximal platform speed of 40 km/h.

Hydraulic cylinders will be used for steering the wheels. Hydraulic cylinders are extremely suitable for precision positioning under high loads with a limited stroke. The hydraulic actuator has a high power/weight ratio which is preferred at locations where there is little space. The stroke of a cylinder is limited which limits the wheel angles

$$\mid \delta_i \mid \leq 45\ ^o \tag{2.5}$$

what coincides with a minimal curve radius of $4\sqrt{2}$ [m]. A hydraulic cylinder will actuate the system on velocity level because the oil flow to the cylinder is determined by the valve input. This poses a limit on the steering speed.

$$\mid \dot{\delta}_i \mid \leq 360\ ^o/s \tag{2.6}$$

Sensors

In this stage of the design, the place and type of sensors can still be chosen freely. Sensors for measuring steering angles and wheel speeds are relatively easy to install. When absolute units, related to the world have to be measured, more advanced sensors have to be used. The sensor quality and costs are depending on required sensor precision and sampling frequency. Local sensors are preferable for high bandwidth and high precision control loops.

The final choice of type and location of sensors will be made in a later stage when the control structure will be defined.

2.5 Servo control

In the previous section, the driving and steering actuators were discussed. Apart from the next control steps, a servo control system for the actuators will be proposed in this section. The wheel speeds will be servo controlled to a reference rotational speed and the wheel steering angles will also be servo controlled. A number of reasons will plead for this servo control approach.

After the modeling of chapter 4, it can be proven that the servo controlled system is stable on velocity level. This automatically means the whole system is detectable, which offers a lot of possibilities for choosing feedback variables. Without the models, this can also be shown by reasoning. If all the wheels have a prescribed velocity and steering angle, they actually do have a prescribed velocity in ATV-fixed x- and y- direction. In total eight speeds while the platform can only have three main velocities. If the wheels do not have matching speeds, some slip will start compensating for this. Finally, the final velocity can be predicted exactly. Other perturbations will all be dampened out since this is a physical system with dampers in the construction.

The ATV is not a holonomic system. In the case of the ATV this means the vehicle is not able to move sideward directly due to limited steering angles. By driving forward and backwards, this sideward movement can be reached with a detour. This is the reason there are no requirements posed on position level. A certain range of velocities can all be obtained directly be the system however. Acceleration demands again can lead to inadmissible velocities. The acceleration demands can be translated to velocity demands on which level the tracking demands are posed. A time delay in velocity equals the same time delay in acceleration, the same applies for magnitude errors. This makes the velocity a good tracking variable.

Driving the wheels directly by a torque would be a fast way to produce force interaction between the road and tyre. However, when the tyre forces become very high, the saturation region of the tyres can be reached and more slip will result in a lower tyre force. This situation is unstable, and with a constant force, this can result in spinning the wheel up to high speeds. Using a servo control has the advantage of protecting the system from getting in this situation.

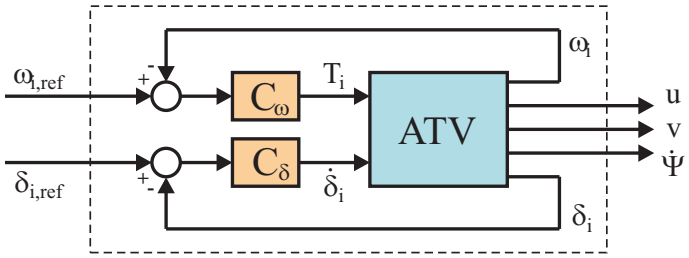

Figure 2.5: Plant H with servo-feedback and new inputs and outputs

The servo control for steering is chosen at a gain of 50. With the actuation at velocity level, the closed loop system from reference steering angle δ_{ref} and real steering angle δ becomes a first order system. The time constant of this first order system τ_{hydr} of 0.02 [s] is typical for this kind of hydraulic systems.

$$\delta_i + \tau_{hydr}\dot{\delta}_i = \delta_{i,ref} \tag{2.7}$$

For the driving controller, a single gain C_ω of $11,000\ Ns/m$ is chosen. The process of obtaining this value is described in appendix D. It is tuned in such a way that the lateral and longitudinal dynamics have approximately the same response time. A longer response time for longitudinal direction would decrease system performance, while a faster response would increase problems with sensor noise and robustness.

Chapter 3

Literature survey

In the automotive industry, large amounts of research has been done in the field of autonomously guided control as well as in vehicle stability improvement. It must be discovered if current control technologies can be applied to the ATV or if a new strategy has to be developed. Therefore, existing control solutions and their belonging models are examined and the goals of each controller design is compared to the ATV control goals. In this chapter, the literature results will be summarized while in the following chapters, models belonging to the tyres and the platform will be examined in more detail. Literature related to specific methods and subjects is referred to in the concerning chapters.

3.1 ABS

Anti-lock Braking System, or ABS, has been installed in cars since the eighties of the last century. At this moment, most modern cars are equipped with ABS as an important safety system. The reasons for using an ABS system are related to tyre properties. Under normal conditions tyres will generate the maximum braking force under a condition of about 15% slip. With higher slip rates, the braking force will reduce. This might result in an unstable situation where wheel-lock easily occurs and a lower braking force is generated. Another unpleasant phenomenon is that at wheel lock, no lateral forces can be generated and the car will slide rudderless unable to avoid obstacles. The high complexity of this control problem is found in the non-linearity of the tyre, in the uncertainty in tyre parameters in changing driving conditions such as icy roads and in difficulties in estimating slip

rates. Quarter-car models as discussed in section 4.1 are mostly used to describe vehicle dynamics for this kind of control problem, control solutions are tried to be found in rule-based control [7] and fuzzy control [8]. Research in the field of tyre state estimation is also done. A similar approach can also be used for traction control.

In extreme situations, traction control and ABS might help avoiding uncontrolled slip. However, the above methods do not produce solutions for the automatic guidance of a vehicle. The advantage using quarter-car models, is that longitudinal and lateral dynamics can be well described with relatively simple models. Yaw, pitch and roll effects can evidently not be showed by the model.

3.2 Single track model steering

In this section, control solutions based on a more advanced model will be discussed. The quarter car model of the last section does not describe yaw dynamics which will often play a critical role in vehicle stability. Single track models are the simplest models that include this effect.

In single track models, the two front and two rear wheels are lumped into single wheels. In this way, a model is obtained which is still comprehensible. Often, the goal of this model is to find a tracking controller while maintaining stability in lateral and yaw directions at high speeds. In the paper of Ackermann [9], various linear and non-linear controllers are designed that can handle both the uncertainty in tyre friction coefficients and vehicle speed. The tyres are modeled as steady state tyres in this investigation.

This model is very suitable for car design. In most cars, only one steering input on both front wheels is available and the driving torque is equally distributed to the rear wheels by a differential. Hence, this model is commonly used in vehicle stability control design. For four wheel driven (4WD) and four wheel steered (4WS) vehicles like the ATV, more control inputs as only steering and driving on single wheels are available. By steering all these inputs separately, a high performance can be obtained. Think for example about differential (tank) steering and shifting torque to the maximum loaded tyre for optimal traction.

3.3 Control of two-track models

The two track model is a more advanced kind of model. Every wheel can now independently drive and steer. Instead of only by steering, yaw compensation is now also possible by differential driving between the left and right wheels. Two kinds of two-track models are primarily used in the literature. The first is a planar model in which the platform only has three DOF's, while the other also includes roll and possibly pitch to resemble suspension dynamics and describe wheel load distribution. Both models are described in appendix E.

Again, the two track model is often used for maintaining stability during extreme steering maneuvers. The two-track model has become more complicated and is also overactuated. In reference [10], this is dealt with by calculating reference tyre forces as a function of driver steering input using a reference model. Afterwards, the generation of these forces is considered a separate problem. These tyre forces are tracked by a controller which compares the reference with the estimated tyre forces. A similar approach is done in reference [11]. Here, a global controller compares vehicle and reference position and gives desired vehicle accelerations as outputs. An optimization step calculates how tyre slips optimally can be distributed among the wheels in a way that reference acceleration constraints are obeyed. With known reference speed and desired slip, wheel speeds and angles are calculated. These variables are tracked separately with servo-controllers.

A completely different approach is presented in [12]. The system is considered multi-DOF and linear in its working area. With this linearized model, standard H_2 and H_∞ control solutions are applied. Both approaches seem to be interesting and will be further discussed in the literature conclusion.

3.4 Conclusion

Previous sections showed that the simplest models and belonging control strategies are not suitable for ATV control design. The quarter-car and lumped wheel approaches cannot incorporate the effect of generating torque by differential driving. In this conclusion, the two-track strategies of section 3.3 will be discussed. Their compatibility with the ATV analyzed and further research will be motivated.

All available two-track models use steady state tyre formulas, sometimes with non-linear slip force characteristics. While driving at high speeds, or

while cornering into the saturation region of the tyres, tyre relaxation length plays a minor role in system responses. This coincides with most control goals which is stabilizing systems in extreme situations to prevent crashes. The most important ATV control goal however, is to obtain a minimal time delay. At speeds at which the ATV is driving of under 40 km/h, tyre relaxation length will start playing a significant role in system responses. Analysis of ADSE [3] showed this effect. For high performance demands as in the ATV, modeling of transient tyres is necessary.

The approach of references [10] and [11] can be used to create a stabilizing 4WS/4WD control strategy under extreme driving close to or in the tyre saturation region. However, the tyres used in the model are not dynamically modeled. It seems difficult to include transient tyres in this control strategy. The maximum achievable control performance with this control strategy for the ATV must be found. An investigation has to show if this control strategy is suitable for ATV control.

The method of reference [12] has no problems including a large number of states and dynamic tyres in the model. With a linear model different control strategies are possible. Dealing with non-linearity of large steering angles and tyre saturation, becomes difficult in this case. The non-linear effect by steering has to be investigated as well as how much tyre saturation will occur.

The above strategies will serve as a basis for the following research. The feasibility of both methods has to be researched, and a final ATV control strategy has to be determined. First of all, in the following chapter, an in-depth investigation of the separate platform and tyre models will be performed to obtain a good understanding of them.

Chapter 4

Dynamic models of the ATV

In the literature, various vehicle models are described. Models suitable for analyzing the ATV dynamics are reproduced and reviewed in this chapter. Different models for the main platform and tyres are combined to complete ATV models. The separate platform models are extensively discussed in appendix E and the tyre models in appendix F.

Three models will be handled in this chapter. The first section will present the relatively simple analytical quarter car model. This model clearly shows how different system parameters influence the system dynamics. Secondly, the planar model including yaw motion and four independent wheels will be used for control design. Finally, a multibody model will be presented for validation purposes. The last two models will be compared in the time and frequency domain.

4.1 Quarter car model

A quarter car model covers the basic dynamics of a wheel and tyre connected to a larger mass. This makes this model very suitable for understanding the basic behavior of a vehicle. For the same reason, the models are analyzed without servo control. A separate model will be used for longitudinal and later dynamics.

In figure 4.1, the inertias for the longitudinal model are decoupled according to Newton-Euler's method. The linear transient tyre model is used, linearized around a constant forward velocity. The equations of motion be-

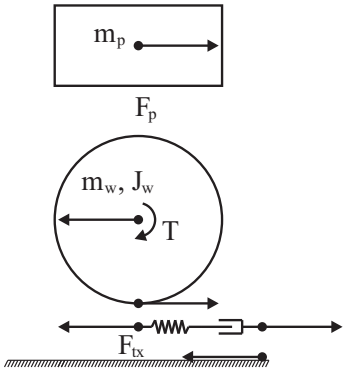

Figure 4.1: Decoupled longitudinal quarter car model

longing to this model are:

$$\begin{aligned} \dot{u} &= \frac{1}{m} F_{tx} \\ \dot{F}_{tx} &= -\frac{C_{fx}}{C_{f\kappa}} |V_{x0}| F_{tx} + C_{fx}(r_e\omega - u) \\ \dot{\omega} &= -\frac{r_e}{J_w} F_{tx} + \frac{1}{J_w} T_m \end{aligned} \tag{4.1}$$

The symbols are also explained in appendices E and F.

When these equations are transformed to the laplace-domain and are rewritten with T_m as input and u as output, the next result is obtained.

$$\frac{u(s)}{T_m(s)} = \frac{1}{\frac{mJ_w}{r_e C_{fx}} s^2 + \frac{mJ_w|V_{x0}|}{r_e C_{f\kappa}} s + mr_e + \frac{J_w}{r_e}} \cdot \frac{1}{s} \tag{4.2}$$

The similarity between this transfer function and the transfer function of a mass-spring system

$$H(s) = \frac{1}{ms^2 + ds + k} \tag{4.3}$$

is obvious. As known from the mass-spring system, the undamped eigenfrequency and dimensionless damping constant of a system are defined as

$$\omega_n = \sqrt{\frac{k}{m}} = 8.1 \ [Hz] \tag{4.4}$$

$$\xi = \frac{d}{2\sqrt{mk}} = 0.18\ [-] \tag{4.5}$$

which gives clear characteristics for this system. Equation 4.2 also shows which elements determine how the transfer from T_m to u looks like. The steady state acceleration is mainly determined by the mass of the platform. The eigenfrequency by the wheel inertia J_w and carcass stiffness C_{fx}. And the damping by the forward velocity V_{x0} and tyre slip stiffness $C_{f\kappa}$.

Figure 4.2 shows the lateral decoupling of the model inertias. Again, the linear transient tyre model is used and there is linearized around a constant forward velocity.

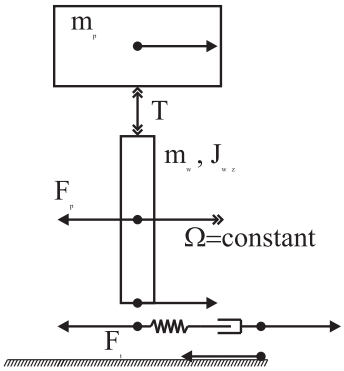

Figure 4.2: Decoupled lateral quarter car model

For the lateral equation of motion, all angles are assumed small and approximated linear.

$$\begin{aligned} \dot{v} &= \frac{1}{m} F_{ty} \\ \dot{F}_{ty} &= -\frac{C_{fy}}{C_{f\alpha}} |V_{x0}| F_{ty} + C_{fy}(V_{x0}\delta - v) \\ \dot{\delta} &= \dot{\delta} \end{aligned} \tag{4.6}$$

The lateral transfer function from steering velocity $\dot{\delta}$ to the lateral velocity v.

$$\frac{v(s)}{\dot{\delta}(s)} = \frac{V_{x0}}{\frac{m}{C_{fy}} s^2 + \frac{m|V_{x0}|}{C_{f\alpha}} s + 1} \cdot \frac{1}{s} \tag{4.7}$$

Whereas, in this case, the system dynamics are:

$$\omega_n = \sqrt{\frac{k}{m}} = 1.3 \ [Hz] \tag{4.8}$$

$$\xi = \frac{d}{2\sqrt{mk}} = 1.09 \ [-] \tag{4.9}$$

The lateral low frequent gain is now dependent on the forward velocity which will, contrary to the vehicle mass, vary during driving. The eigenfrequency is dependent on the platform mass m and the lateral tyre carcass stiffness C_{fy}. The damping is again mostly determined by forward velocity V_{x0} and the tyre slip stiffness $C_{f\alpha}$.

It is interesting to see that the system damping is in both cases dependent on the varying vehicle speed. In the lateral case, the system gain is even dependent on the forward velocity. A significant difference in eigenfrequency can be noticed. The lateral eigenfrequency will be determined by the whole ATV mass being suspended on the tyre carcass stiffness. While in the longitudinal case, the rotating wheels decouple this system and the eigenfrequency will be mainly determined by wheel inertia suspending on longitudinal tyre spring stiffness. The longitudinal system has a much higher eigenfrequency and is therefore much easier to control. In servo control this effect cannot been seen. Therefore, this model analyzed in open loop.

4.2 Planar model

For control design it is desired to obtain the simplest analytical model that contains as much possible system properties. The planar and pitch/roll platform models are both derived by hand in appendix E. This appendix also showed that the pitch/roll model did not represent the pitch and roll behavior well. The multibody model is assumed to resemble real dynamics sufficiently, but is considered too complicated for a fist modeling step. The tyres will be modeled by the linear transient tyre model of appendix F. This model is accurate within the linear slip region and comprehends the tyre stiffness. Later, in subsection 4.5, the influence of this tyre stiffness on the complete behavior will be analyzed.

The planar ATV model will be modeled by Newton-Euler equations. The first set of equations describe the motion of the platform and is based on

equation E.1.

$$\begin{aligned}
\dot{u} &= -v\dot{\Psi} + 1/m(F_{cmx1} + F_{cmx2} + F_{cmx3} + F_{cmx4}) \\
\dot{v} &= +u\dot{\Psi} + 1/m(F_{cmy1} + F_{cmy2} + F_{cmy3} + F_{cmy4}) \\
\ddot{\Psi} &= s/J(-F_{cmx1} - F_{cmx2} + F_{cmx3} + F_{cmx4}) + \dots \\
&\quad a/J(F_{cmy1} - F_{cmy2} - F_{cmy3} + F_{cmy4})
\end{aligned} \tag{4.10}$$

Where F_{cmxi} and F_{cmyi} the longitudinal and lateral force in the corner modules in ATV-fixed coordinates.

The differential equations of the tyre are modeled according to equation F.15. A similar expression is used for the y-direction. The wheel is modeled as a simple rotational inertia and the steering dynamics behaves as a first order system as in equation 2.7. The self aligning torque is not modeled.

$$\begin{aligned}
\dot{u}_{ti} &= -\frac{C_{fx}}{C_{f\kappa}}|V_{xi}|u_{ti} - (V_{xi} - \omega_i r_e) \\
\dot{\omega}_i &= C_\omega/J_w(\omega_i - \omega_{i,ref}) - r_e C_{fx} u_{ti}/J_w \\
\dot{v}_{ti} &= -\frac{C_{fy}}{C_{f\alpha}}|V_{xi}|v_{ti} - V_{syi} \\
\dot{\delta}_i &= \frac{1}{\tau_h ydr}(\delta_{i,ref} - \delta_i)
\end{aligned} \tag{4.11}$$

With V_{xi} and V_{syi} the longitudinal and lateral wheel velocities in wheelcarrier-fixed coordinate system. V_{xi} and V_{syi} need to be substituted in the previous equation which produces numerous nonlinear terms in the equations of motion.

$$\begin{bmatrix} V_{xi} \\ V_{syi} \end{bmatrix} = \begin{bmatrix} \cos(\delta_i) & \sin(\delta_i) & 0 \\ -\sin(\delta_i) & \cos(\delta_i) & 0 \end{bmatrix} \left(\begin{bmatrix} u \\ v \\ 0 \end{bmatrix} + \begin{bmatrix} 0 \\ 0 \\ \dot{\Psi} \end{bmatrix} \times \begin{bmatrix} r_{xi} \\ r_{yi} \\ 0 \end{bmatrix} \right) \tag{4.12}$$

F_{cmxi} and F_{cmyi}, of equation 4.10 are also not directly available as states. Therefore, another transformation is needed. Again, nonlinear terms are introduced.

$$\begin{bmatrix} F_{cmxi} \\ F_{cmyi} \end{bmatrix} = \begin{bmatrix} \cos(\delta_i) & -\sin(\delta_i) \\ \sin(\delta_i) & \cos(\delta_i) \end{bmatrix} \begin{bmatrix} C_{fx} u_{ti} \\ C_{fy} v_{ti} \end{bmatrix} \tag{4.13}$$

Above equations build up the whole system. The substitutions are performed with MATLAB's symbolic toolbox. The platform contains three

states (eq. 4.10) and each corner module has four states (eq. 4.11). The complete system contains 19 states. The complete equations can be found in appendix G.

The equations are used to create both a nonlinear and linear system. The linear system matrices are obtained by differentiating the system equations to the state variables. For fast calculation times, the nonlinear equations are converted to a dll-file.

4.3 Multibody model

The multibody model will be used for validation. A complete model is therefore desired which makes a multibody modeling approach very suitable. The Simmechanics model of appendix E is extended with wheels and tyres. The wheels are modeled as rigid disks and the MF-Tyre/Delft-Tyre tyre model [6] is used as described in appendix F.

For analysis of the multibody model, the model is linearized. The model will be fed with realistic inputs and simulated until a steady-state condition is reached. A snapshot of the states is taken, around which the system will be linearized. Each block within the linearization path will be analytically linearized individually first. When no analytical linearization is possible, the numerical perturbation method will be used, see reference [14]. Afterwards the complete linearized system will be connected.

4.4 Kinematic steering

Two linear systems are now derived. However, analyzing an 8×3 system is not an easy task. The system response caused by a single reference wheel angle change is not realistic. Some combinations of steering angles will even cause the ATV to stop with blocked wheels. In general, a certain combination of wheel angles and wheel speeds is feasible. In this subsection, a practical set of steering signals will be discussed.

If the ATV would be massless and no accelerating force had to be transferred by the tyres, the tyres would have to roll without any slip. This situation can be calculated analytically and is named kinematic steering of the ATV. If the forward velocity u, lateral velocity v and rotational velocity $\dot{\Psi}$ are known, the local velocity at the tyre can be calculated with equation 4.12

(use $\delta_i = 0$). For rolling without slip, the following wheel speeds and angles have to apply.

$$\omega_{i,kinematic} = \sqrt{{V_{xi}}^2 + {V_{syi}}^2} \tag{4.14}$$

$$\delta_{i,kinematic} = \arctan\left(\frac{V_{syi}}{V_{xi}}\right) \tag{4.15}$$

In other words. If the reference trajectory $\underline{r}$ is know, a nonlinear function $f_{kinematic}$ which calculates the system kinematic inputs $\underline{u}$ exists.

$$\underline{u} = \underline{f}_{kinematic}(\underline{r}) \tag{4.16}$$

Where the reference $\underline{r}$ is defined as

$$\underline{r} = \begin{bmatrix} u_{ref} & v_{ref} & \dot{\Psi}_{ref} \end{bmatrix}^T \tag{4.17}$$

and the system inputs $\underline{u}$ are defined as

$$\underline{u} = \begin{bmatrix} \omega_{1,ref} & \delta_{1,ref} & \omega_{2,ref} & \delta_{2,ref} & \omega_{3,ref} & \delta_{3,ref} & \omega_{4,ref} & \delta_{4,ref} \end{bmatrix}^T \tag{4.18}$$

To use this kinematic steering in combination with the linear model, $f_{kinematic}$ is linearized around a working point.

$$R = \left.\frac{d\underline{f}_{kinematic}}{d\underline{r}}\right|_{\underline{r}_0} \tag{4.19}$$

Where R is an 8×3 system. When R is combined with the servo controlled linearized AGS, $H(s)$, the 3×3 system $H \cdot R$ is created.

As an example, the kinematic steering matrix R for a forward velocity u of 5 m/s is given. Notice that the values of the first column equal $1/r_e$ and the values of the second column equal $1/u_0$.

$$R\begin{bmatrix} 5 & 0 & 0 \end{bmatrix} = \begin{bmatrix} 1.877 & 0 & -5.31 \\ 0 & 0.2 & 0.5657 \\ 1.877 & 0 & -5.31 \\ 0 & 0.2 & -0.5657 \\ 1.877 & 0 & 5.31 \\ 0 & 0.2 & -0.5657 \\ 1.877 & 0 & 5.31 \\ 0 & 0.2 & 0.5657 \end{bmatrix} \tag{4.20}$$

4.5 Comparison

Numerous models have been treated in this chapter. This comparison summarizes the differences and the similarities of the discussed models.

The planar model does not contain pitch/roll dynamics and tyre saturation, while the multibody model has all the effects included. The last two items of the list cannot be seen in the linearized version of the models. Steering nonlinearity and tyre saturation limits only the working range of the models. In this comparison, the effect of the Pitch/Roll dynamics and the tyre stiffness is to be investigated. The planar model does not include pitch/roll dynamics while the multibody model does. The transient tyre behavior can be turned off in the MF-tyre model and the tyre stiffness can be increased by a number of orders in the planar model. Four linear models are obtained in this way. A summary of the different models is made in table 4.1.

Table 4.1: Models summary

	Quarter car	Pitch/Roll	Planar	Multibody
states	6	7	19	40
Ψ freedom	No	Yes	Yes	Yes
pitch/roll	No	Yes	No	Yes
transient tyres	Yes	n.a.	Yes	Yes
nonlinear tyres	No	n.a.	No	Yes
nonlinear steering	No	n.a.	Yes	Yes
camber effect tyres	No	n.a.	No	Yes
self aligning torque tyres	No	n.a.	No	Yes

In figure 4.3, the step responses of the planar and multibody models are plotted. The models are pre-multiplied with the kinematic steering matrix R to obtain more understandable results.

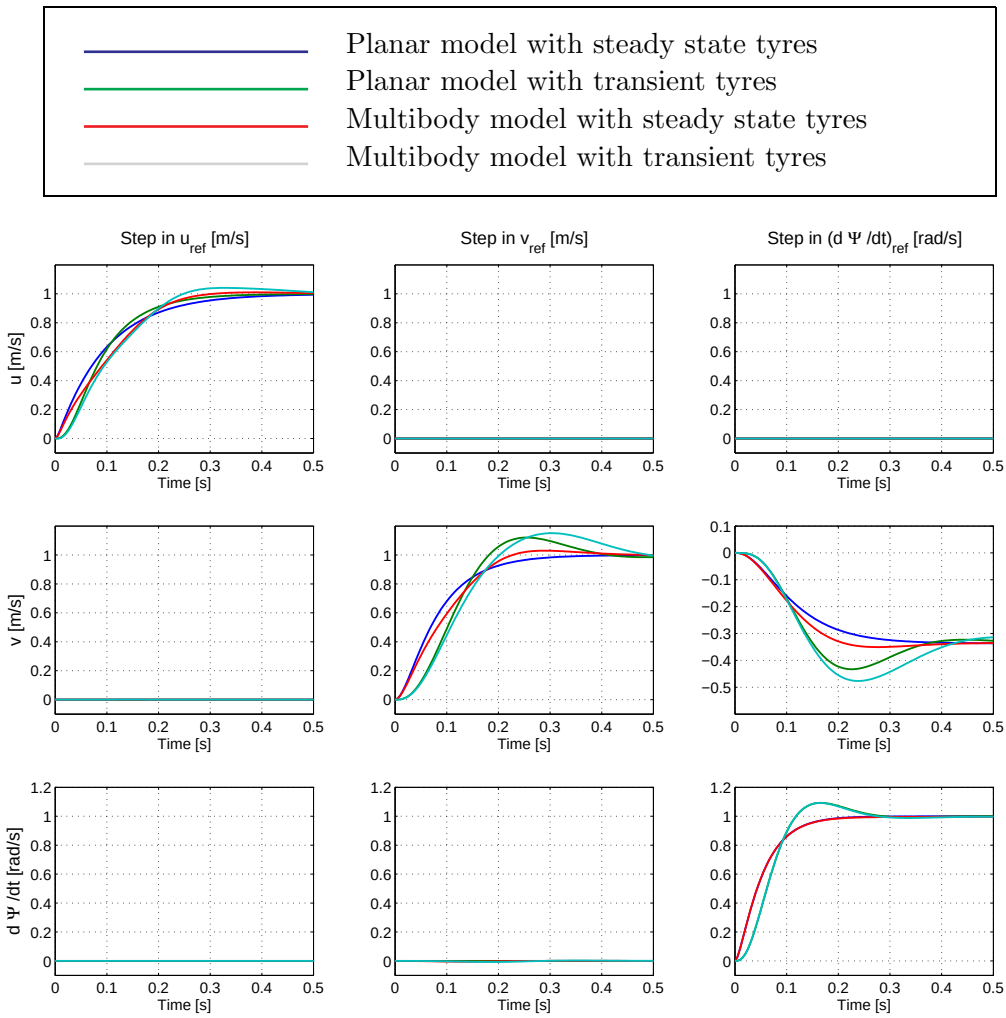

Figure 4.3: Step responses for linearized systems with kinematic input reference $H \cdot R$

Figure 4.3 shows a clear difference between the four models. Especially in the transfer from input v_{ref} to output v, differences are visible. This makes sense because rotating the wheel will directly excite the system dynamics. The servo controller will more or less provide a constant torque that almost directly generates a force on the ground, which makes the longitudinal transfer step response more smooth. Notice that the initial response and steady state value for the planar and the multibody models are equal. This gives confidence in the models because neither of both model components' are used in the other model. Furthermore, it can be seen that the planar and multibody model give exactly the same results for the transfer from $\dot{\Psi}_{ref}$

to $\dot{\Psi}$. No pitch or roll is generated because of the zero net force and only resulting torques around the z-axis. A reference yaw rotation will result in a lateral velocity because of the centrifugal acceleration causing the ATV to slip. At last, a small response is seen in transfer form v_{ref} to $\dot{\Psi}$ in the multi-body model caused by self aligning torques, wheel inertia's and gyroscopic torques.

The steering is shown to be the most dependent on system dynamics. Therefore, the frequency response form input v_{ref} to output v is depicted in figure 4.4. In the magnitude plot, two lines with a magnitude offset of 5% are drawn to depict the performance constraints. Similarly, in the phase plot, the 40 ms performance requirement is drawn as a dotted line. A 20 ms and 60 ms phase line is also drawn.

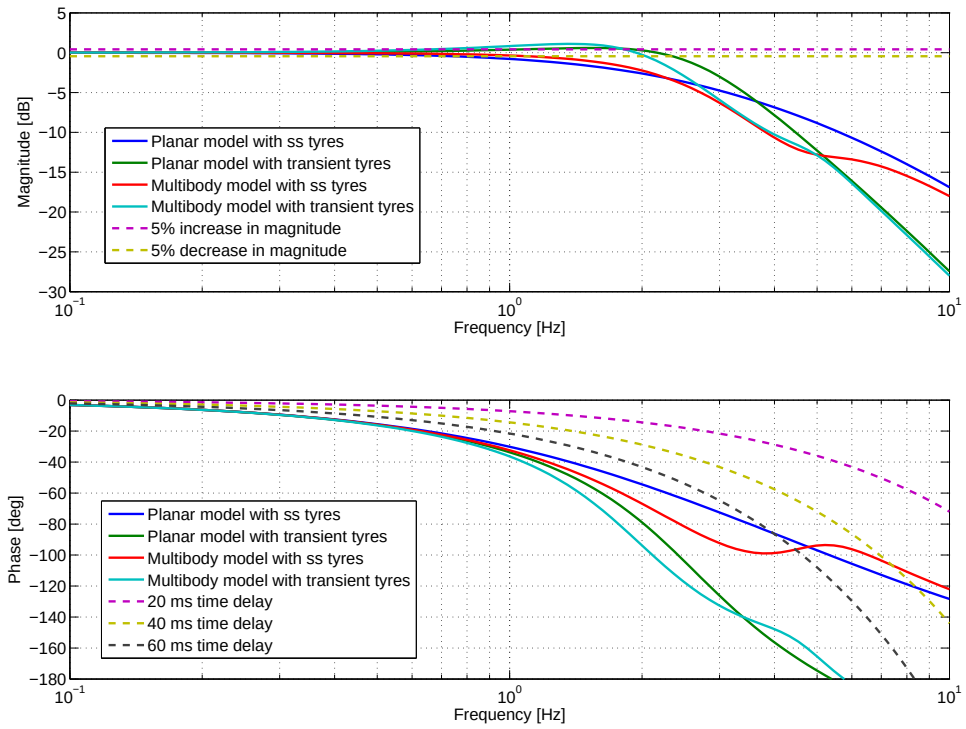

Figure 4.4: Bode diagram of $H \cdot R_{(2,2)}$: from v_{ref} to v using kin. steering

Up to the frequency of 2 Hz. both pitch/roll dynamics and transient tyre behavior start playing a significant role. Especially the tyre stiffness is crucial in phase-delay. A controller which will compensate for this effect is necessary to satisfy control goals.

Chapter 5

Overactuation

One of the main difficulties of designing a 4WD/4WS vehicle control system is that the vehicle is overactuated. There are eight control inputs while only three variables need to be controlled. In this chapter, the way to handle this overactuation of the ATV is investigated.

5.1 Control allocation

In the literature, control allocation is frequently used to deal with actuator redundancy as described in references [16] and [17]. Here, the control allocation is seen as a separate task of distributing the desired control action over the actuators. This is depicted in figure 5.1.

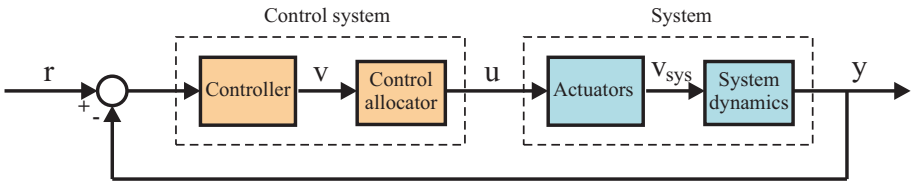

Figure 5.1: Scheme of control allocation

Assume that the B-matrix of the overactuated linear system

$$\dot{x} = Ax + Bu \tag{5.1}$$

has a rank k lower than the number of inputs m. This means that there exists a nullspace of dimension $m - k$ in which the inputs can be varied

without affecting the states of the system. Control allocation can solve this redundancy by a transformation of the form $u = Q \cdot v$. The new system equation becomes

$$\dot{x} = Ax + BQv \tag{5.2}$$

where BQ has now full column rank. The choice of Q is often based on actuator constraints. When actuator dynamics start influencing the system, this input factorization has to be used with care. The next equation with first order actuator dynamics will clarify that.

$$\begin{bmatrix} \dot{x} \\ \dot{u} \end{bmatrix} = \begin{bmatrix} A & B \\ 0 & -B_a \end{bmatrix} \begin{bmatrix} x \\ u \end{bmatrix} + \begin{bmatrix} 0 \\ B_a \end{bmatrix} u^{cmd} \tag{5.3}$$

The matrix B_a will have full column rank since every input affects a separate actuator and thus separate system states. By assuming the actuator dynamics have approximately the same fast time constant, the input transformation $u^{cmd} = Q \cdot v^{cmd}$ is permitted. Servo control on actuator level is regularly used to obtain the required fast servo behavior required for control allocation. Note that the reference actuator positions u^{cmd} are now allocated instead of the real actuator positions u.

In the case of the ATV, every control input has a unique influence on the states of the system at velocity level as in equation 5.3. The direct transformation as in equation 5.2 is therefore not possible. When only the dynamics of the platform without the wheels and tyres is analyzed, such a transformation is possible, however. The platform is now force actuated with the redundancy shown in figure 5.2. Four forces with both a longitudinal and lateral component can be produced while only the sum of the longitudinal forces $\sum F_x$, the sum of the lateral forces $\sum F_y$ and the sum of the torques $\sum T_z$ influence the system dynamics. It has to be assumed that a servo controller can build up the allocated forces relatively quick compared to the global controller to obtain the notation of equation 5.3.

Instead of the eight separate force components, the new control input v of the system of equation 5.2 becomes

$$v = \begin{bmatrix} \sum F_x & \sum F_y & \sum M_z \end{bmatrix} \tag{5.4}$$

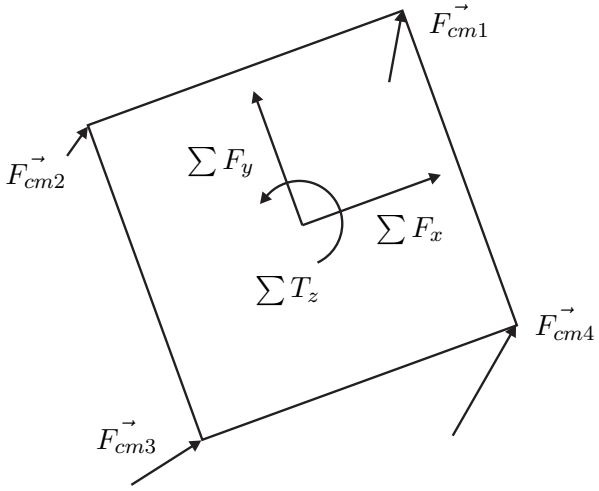

Figure 5.2: Sum of the planar forces

5.2 Force allocation strategies

Strategy 1

Tyres can typically produce a limited amount of horizontal force. The maximal horizontal force divided by the vertical force is denoted by the symbol μ. When the relative tyre force reaches this value of μ, the amount of slip will increase while the vertical force stays constant or even decreases as explained in appendix F. During control, this unstable situation should be avoided for every tyre. A first strategy to allocate the forces would be to keep the relative tyre force equal for every tyre.

$$\left|\frac{F_{cm1}}{F_{tz1}}\right| = \left|\frac{F_{cm2}}{F_{tz2}}\right| = \left|\frac{F_{cm3}}{F_{tz3}}\right| = \left|\frac{F_{cm4}}{F_{tz4}}\right| \tag{5.5}$$

The reference force constraint has to be obeyed at the same time. It states that the sum of forces and torque have to resemble the reference forces and torque.

$$\begin{aligned} F_{cmx1} + F_{cmx2} + F_{cmx3} + F_{cmx4} &= \sum F_x \\ F_{cmy1} + F_{cmy2} + F_{cmy3} + F_{cmy4} &= \sum F_y \\ 2\sqrt{2}[-F_{cmx1} + F_{cmy1} - F_{cmx2} - F_{cmy2} \ldots & \\ \quad + F_{cmx3} - F_{cmy3} + F_{cmx4} + F_{cmy4}] &= \sum T_z \end{aligned} \tag{5.6}$$

A technique like this is used in reference [11] and does have as advantage that the relative tyre forces are all equal and in limit situations all tyres saturate the same amount. However, there are also clear disadvantages. Finding the solution to equation 5.5 under constraint of equation 5.6 is not an easy task. An optimization algorithm needs to be used while the problem is not-convex. This means several local minima may exist and never can be determined if the real optimum is found. Besides, this optimization is a computational intensive process. Furthermore the found solution is not minimal in energy norm. When looking at figure 5.2, common sense tells us that actuator 2 can never be contributing much to the desired sum of forces and torque. Hence, a low produced force is desired by this tyre. Strategy one forces it to be identical in amplitude as the other tyre forces.

Strategy 2

In strategy 2, the minimal energy solution for the tyre force distribution problem will be attempted to be found. This coincides with the following minimization.

$$\min_{F_{cmi}} \left(\left| \frac{F_{cm1}}{F_{tz1}} \right|^2 + \left| \frac{F_{cm2}}{F_{tz2}} \right|^2 + \left| \frac{F_{cm3}}{F_{tz3}} \right|^2 + \left| \frac{F_{cm4}}{F_{tz4}} \right|^2 \right) \tag{5.7}$$

Subject to the linear constraint of equation 5.6.

This quadratic minimization with linear constraints can be solved in one matrix inversion using Karish-Kuhn-Tucker (KKT) conditions [18]. This makes it a computational fast procedure and suitable for the use in a real-time control system. A more elaborate formulation of the minimization procedure can be found in appendix H.

Strategy 3

The most direct approach for distributing the tyre forces is strategy 3. Here, the sum of the longitudinal forces is only built up out of equally distributed longitudinal forces. The sum of the lateral forces is only built up out of equally distributed lateral forces. The sum of torques is built up out of equally distributed forces directed perpendicular to the line connecting the center of gravity and the point where the force originates. These eigenforms are shown in figure 5.3.

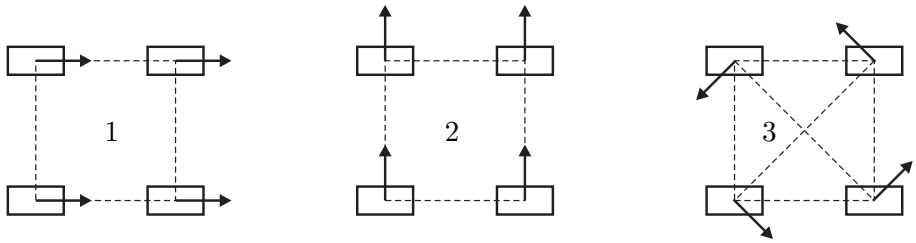

Figure 5.3: Tyre force eigenforms according to allocation strategy 3

The transformation belonging to these eigenforms is

$$\underline{F_{cmi}} = \begin{bmatrix} F_{cmx1} \\ F_{cmy1} \\ F_{cmx2} \\ F_{cmy2} \\ F_{cmx3} \\ F_{cmy3} \\ F_{cmx4} \\ F_{cmy4} \end{bmatrix} = \begin{bmatrix} 1/4 & 0 & -1/(16\sqrt{2}) \\ 0 & 1/4 & +1/(16\sqrt{2}) \\ 1/4 & 0 & -1/(16\sqrt{2}) \\ 0 & 1/4 & -1/(16\sqrt{2}) \\ 1/4 & 0 & +1/(16\sqrt{2}) \\ 0 & 1/4 & -1/(16\sqrt{2}) \\ 1/4 & 0 & +1/(16\sqrt{2}) \\ 0 & 1/4 & +1/(16\sqrt{2}) \end{bmatrix} \cdot \begin{bmatrix} \sum F_x \\ \sum F_y \\ \sum T_z \end{bmatrix} \tag{5.8}$$

This calculation is the fastest and simplest of the three. In the case where all vertical tyre forces are identical $F_{tz1} = F_{tz2} = F_{tz3} = F_{tz4}$, strategy 2 and 3 even give the exact same wheel force distribution. Working out strategy 2 shows the same transformation matrix. It can be concluded that both strategy 2 and 3 are suitable as control allocation methods. When a lot of vertical wheel load shifting occurs, method two is preferable.

5.3 Actuator dynamics

Three strategies for control allocation have been investigated. All strategies distribute control action on tyre force level. The ATV inputs are reference wheel speeds and steering angles, however. To make this strategy work, servo controllers need to be implemented which can track a force. Measuring or estimating tyre forces is already a difficult taks itself. Because of the interaction between the corner models this seems to require an universal controller for the whole vehicle. In this section an open-loop method comparable to the design of of Leenen [11] is tried. The maximum attainable performance of this open-loop allocation controller will be investigated in this section.

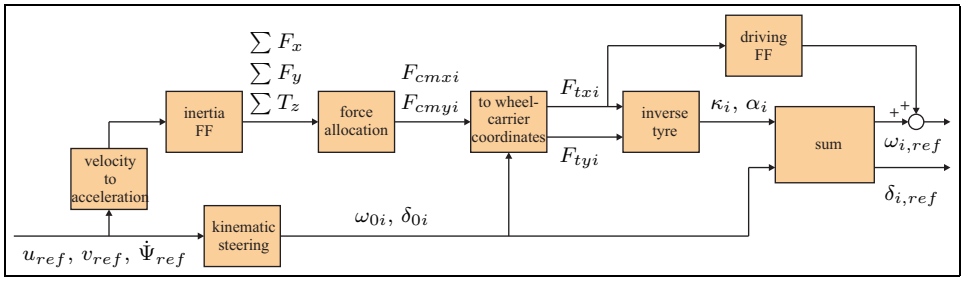

Figure 5.4: Scheme of the feed-forward allocation controller $F(s)$

The allocation controller is based on the *kinematic steering block* as described in subsection 4.4. The difference with kinematic steering is that a little offset in steering and driving is included to compensate for predicted slips. To calculate these slips, the next steps are taken.

The *velocity to acceleration block* uses equation E.3 to calculate the reference accelerations. To prevent differentiating problems, the differentiator has a high frequency cut-off. This frequency is an order higher that the required performance frequency of 2 Hz. The accelerations are multiplied with the ATV inertia's to calculate the total required acceleration forces in the *inertia FF block*. The total required forces are distributed by the *force allocation block* and converted to the wheelcarrier axis-system by the *to wheelcarrier coordinates block*. The desired wheel slips are calculated by the *inverse tyre block*. This block contains the multiplications of $1/C_{f\kappa}$ for longitudinal force-slip conversions and $1/C_{f\alpha}$ for lateral force-slip conversion. In the *sum block*, $\omega_{i,ref}$ is calculated according to equation F.4 and α_i and δ_{i0} are summed to obtain $\delta_{i,ref}$. An additional *driving FF block* is added to improve longitudinal performance by giving a force feed-forward to the wheel speed servo controller. This is done by the multiplication of R_e/C_ω.

The nonlinear allocation controller is also linearized in Matlab/Simulink to make linear analysis possible. Afterwards, the controller is connected in series with different linearized ATV models. The lateral dynamics showed the slowest step responses. Because of the driving feed-forward which helps the servo control, lateral dynamics have become relatively fast. Another interesting effect is that the lateral speed in the case of a constant yaw velocity will become zero. The allocation controller compensates for the expected centrifugal force. The frequency response of the performance limiting transfer from v_{ref} to v are plotted in figure 5.5.

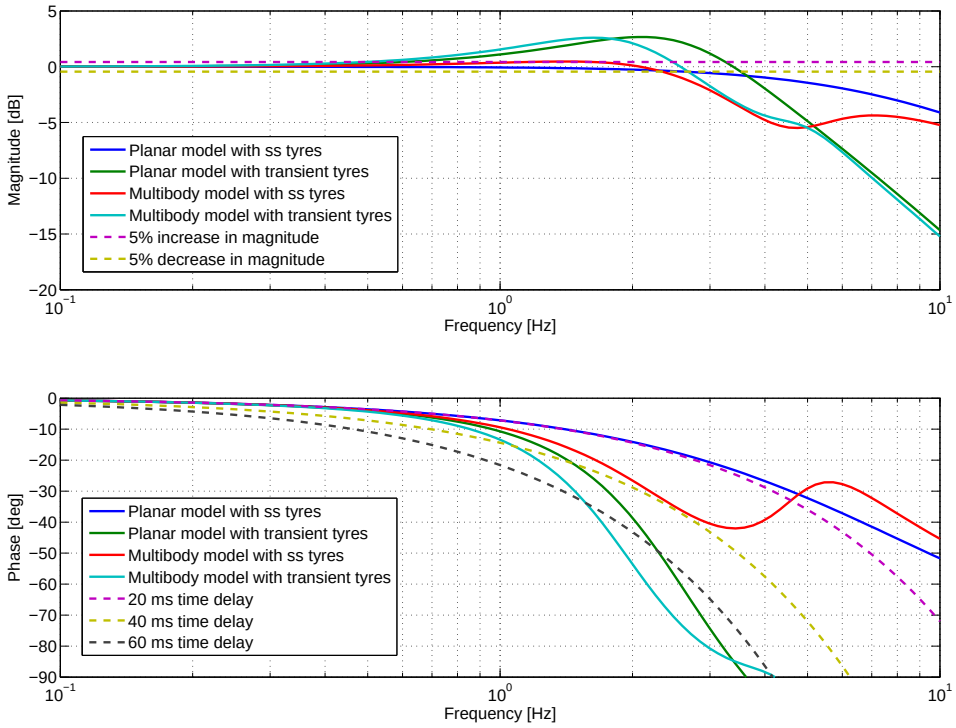

Figure 5.5: Bode diagram of $H \cdot F_{(2,2)}$: from v_{ref} to v using allocated steering

Much faster responses are obtained compared to the responses with the kinematic steering of figure 4.4. Still, the specifications for the maximum time delay of 40 ms up to 2 Hz are trespassed for the models including tyre dynamics. This allocation controller is able to compensate for tyre slip but not for tyre and actuator dynamics.

A more advanced controller is required to meet the control objectives. Obtaining lower response times by placing $H \cdot F$ in another control loop will obtain a complicated control structure and rises questions about how well the tyre forces are still distributed. Using tyre force servo controllers instead of this open-loop approach also results in a complicated control structure. A new strategy for an advanced controller will be presented in chapter 6.

Chapter 6

Control structure

In this chapter, the structure of the ATV controller will be determined. The control structure forms the basis for further control design and mainly determines the final behavior of the controlled system.

The previous chapter showed that conventional allocation techniques did not offer satisfying results. An alternative for these techniques will be given in the first section. With this alternative, control action can be allocated while taking the actuator dynamics into account. The newly defined plant P with its input and output choice is analyzed in the second part of this chapter. An initial control setup is also offered. Practical application problems of the first control setup and the final control structure will be presented in section three.

6.1 Force allocation

One of the difficulties in controlling the ATV is the overactuation of the vehicle. A number of allocation strategies are given in chapter 5. A major disadvantage has been shown to be the inability of the allocation techniques to incorporate the actuator dynamics in the controller. A way to do this will be presented in this section.

Strategy 3 imposed a number of allowable wheel force combinations. All longitudinal tyre forces and all lateral tyre forces are allowed. The situation where all tyre forces are directed counterclockwise perpendicularly to the line between their point of application and the COG of the ATV is also

allowed. These eigenforms were depicted in figure 5.3. The values of the wheel force x- and y-components are collected in a vector which is scaled to one. In this way, three orthogonal vectors of eight elements with unit length are obtained. Every linear combination of these three vectors is allowed. The main problem is to have these forces produced by the servo controllers.

Linear algebra posits that 5 independent vectors exist in the 8 dimensional space which are all orthonormal to the 3 original vectors and each other. Stating the wheel forces have to be in the space spanned by the original three vectors is identical to stating that the forces are not allowed to be in the space covered by the 5 orthonormal vectors. The space spanned by the five orthonormal vectors can be said to be all combinations of 'fighting forces'. The five fighting forces vectors can be chosen in various combinations by matrix-sweeping. In figure 6.1, a more pragmatic approach with recognizable fighting forces is chosen.

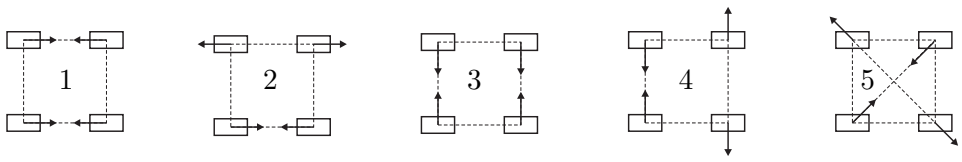

Figure 6.1: Fighting tyre force directions

Tyre forces are directly related to system states and can theoretically be measured. Linear combinations of these forces according to the shapes of figure 6.1 result in five numbers which indicate how many fighting forces exist. These five numbers or variables are desired to be tracked to zero. When this is combined with the three performance variables which have to be tracked, exactly eight controlled variables are created. With the eight inputs of the system, this system is not overactuated nor underactuated. The forces will now be allocated by prohibiting the undesired forces while the controller has no problems incorporating tyre dynamics for optimal velocity tracking.

One problem in using the tyre forces from system states is that in this model the tyre forces are modeled in the wheelcarrier reference frame while fighting forces are defined to be in the ATV-fixed reference frame. This difference causes an offset of the fighting forces directions of figure 6.1 during cornering. For the next part of this thesis, the following assumption is made:

$$F_{cmxi} \approx F_{txi} \tag{6.1}$$

$$F_{cmxy} \approx F_{tyi} \tag{6.2}$$

For practical reasons all tyre forces are first normalized by the nominal vertical tyre force of 19620 N. Normalized tyre forces can never exceed the value of $\mu \cdot F_{tz}/F_{zN}$ and therefore mostly have a value lower than one. Afterwards, the tyre forces will be multiplied with the unit length vectors of the fighting forces forms.

$$\underline{F_{tf}} = \begin{bmatrix} F_{tf1} \\ F_{tf2} \\ F_{tf3} \\ F_{tf4} \\ F_{tf5} \end{bmatrix} = \frac{1}{F_{zN}} \begin{bmatrix} -1/2 & 1/2 & 0 & 0 & -1/\sqrt{8} \\ 0 & 0 & -1/2 & 1/2 & -1/\sqrt{8} \\ 1/2 & -1/2 & 0 & 0 & -1/\sqrt{8} \\ 0 & 0 & -1/2 & -1/2 & +1/\sqrt{8} \\ 1/2 & 1/2 & 0 & 0 & +1/\sqrt{8} \\ 0 & 0 & 1/2 & 1/2 & +1/\sqrt{8} \\ -1/2 & -1/2 & 0 & 0 & +1/\sqrt{8} \\ 0 & 0 & 1/2 & -1/2 & -1/\sqrt{8} \end{bmatrix}^T \cdot \begin{bmatrix} F_{tx1} \\ F_{ty1} \\ F_{tx2} \\ F_{ty2} \\ F_{tx3} \\ F_{ty3} \\ F_{tx4} \\ F_{ty4} \end{bmatrix} \tag{6.3}$$

Where F_{zN} the nominal vertical tyre load and F_{tf} the dimensionless fighting tyre force.

6.2 Plant definition

With the proposed output changes the next 8×8 plant P is defined. P contains the servo controlled ATV with the four reference wheel speeds and reference wheel angles as inputs. The outputs are the three velocities in the horizontal plane and the five dimensionless fighting tyre forces. The three velocities have to be tracked according to the specifications and the fighting tyre forces have to be as small as possible.

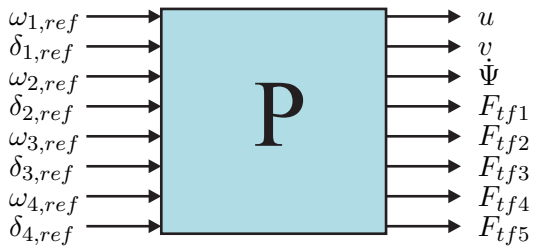

Figure 6.2: ATV inputs and outputs

Van De Wal states in [19] that the selection of inputs and outputs will have significant influence on the final control result that can optimally be

obtained. The new plant which is created with the output transformation intuitively 'feels' well defined. To continue with the next control design steps, this needs to be confirmed mathematically.

The system has an observability matrix of rank 19 which equals the total number of states. A completely observable system is not required in this case because every system state is stable. Independently of the number of observable states, the system will always be detectable. The system is completely controllable as well.

State observability and controllability do not guaranty the possibility for good control of the system. Input-output controllability needs to be analyzed for this purpose. This is done by looking at the singular values of the system.

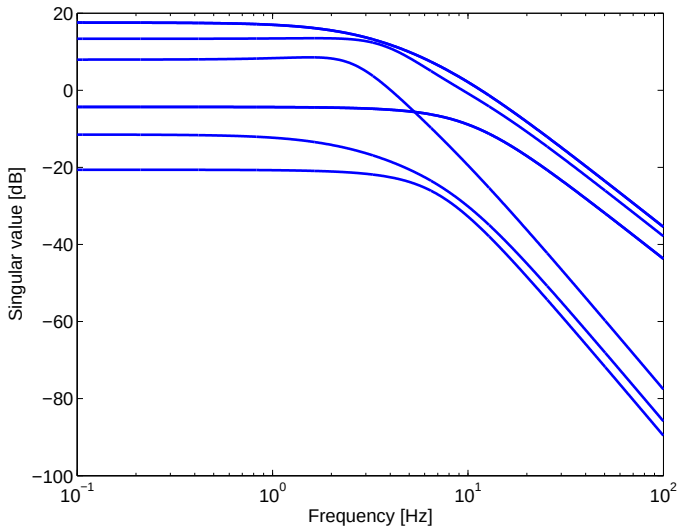

Figure 6.3: Singular values of the ATV planar plant

The singular values of the system as a function of the frequency $\sigma(P(j\omega))$ are plotted in figure 6.3. The lowest singular value $\underline{\sigma}(P(j\omega))$ is relatively close to the other singular values, which means the different outputs can be manipulated independently. The condition number of a system indicates the fraction between the highest and the lowest singular value. For this system, the condition number at low frequencies is $\kappa(P(0)) = 81$. Main amplitude differences are caused by a higher sensitivity for steering than driving at the inputs and a higher sensitivity for fighting forces and a very low yaw velocity response at the outputs.

It is proven that the inputs and outputs of the 8×8 plant P of figure 6.2 are well-chosen. Controlling the system with the well known feedback controller C of figure 6.4 is possible.

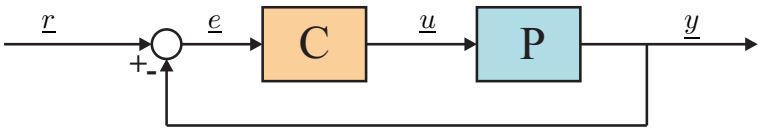

Figure 6.4: Standard feedback controller

Where the reference $\underline{r}$, error $\underline{e}$, input signal $\underline{u}$ and output $\underline{y}$ for this specific system are defined as:

$$
\begin{aligned}
\underline{r} &= \begin{bmatrix} u_{ref} & v_{ref} & \dot{\Psi}_{ref} & 0 & 0 & 0 & 0 & 0 \end{bmatrix}^T \\
\underline{e} &= \begin{bmatrix} e_u & e_v & e_{\dot{\Psi}} & -F_{tf1} & -F_{tf2} & -F_{tf3} & -F_{tf4} & -F_{tf5} \end{bmatrix}^T \\
\underline{u} &= \begin{bmatrix} \omega_{1,ref} & \delta_{1,ref} & \omega_{2,ref} & \delta_{2,ref} & \omega_{3,ref} & \delta_{3,ref} & \omega_{4,ref} & \delta_{4,ref} \end{bmatrix}^T \\
\underline{y} &= \begin{bmatrix} u & v & \dot{\Psi} & F_{tf1} & F_{tf2} & F_{tf3} & F_{tf4} & F_{tf5} \end{bmatrix}^T
\end{aligned}
$$

6.3 Measurement estimation

A major problem of using tyre forces as measured variables is that they are incredibly hard to measure. No sensors are available neither can a satisfying alternative solution be found in the literature. The most sensible solution for determination of the output $\underline{y}$ of a detectable system like the ATV is the use of an estimator. With this strongly nonlinear system, the estimation filter must become nonlinear as well.

Estimating filters use both prediction and measurement data. Depending on the quality of the measurements, a certain weight will be given in updating the predictions with measurement data. It is important to determine which variables can be measured for updating the system states. As stated before, the velocities are relatively hard to measure accurately. With the stable property of the system, using measurement data for updates would not add much improvement to the estimated velocities. The only variables which can be measured accurately are the wheel speeds and wheel angles. The wheel angles are already estimated very accurately because of the stable

first order dynamics. Only the wheel speeds can add some value to the estimation model.

To produce a complete estimator with tuning effort and practical complications such as measurement cables for only this little profit is not considered to be worthwhile. A stable model will be used as an estimator. Each state variable will be purely estimated based on the planar model derived in chapter 4. The next control scheme is obtained, where $\underline{y}^*$ is the estimated output.

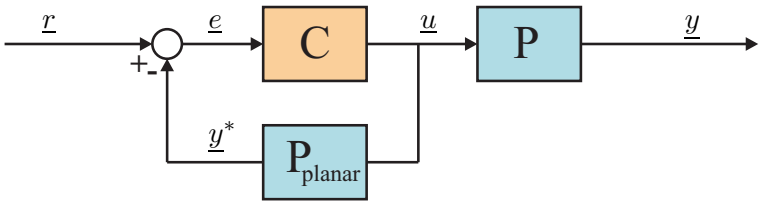

Figure 6.5: Control structure

Figure 6.5 shows the implementation of the feedback loop including estimating filter. No outputs are measured, and both the controller's and the planar model's responses will be computed internally when applied in a real control system. The transfer function from reference $\underline{r}$ to control output $\underline{u}$ using the linearized models equals the control sensitivity defined as:

$$\frac{C}{1 + P_{planar}C} \approx P_{planar}^{-1} \; if \; C \uparrow \tag{6.4}$$

Below the bandwidth where $P \cdot C \gg 1$, approximately P^{-1} is created by the feedback loop. The plant is inverted up to a certain frequency by implementing the control system as above such that $\frac{\underline{y}}{\underline{r}} \approx P \cdot P^{-1} = I$.

As long as the controller is designed robustly enough for a range of systems, the controller will stabilize the system for different working points. The controller tracks the vehicle at different speeds and during straight line driving, crabbing or cornering. During all these maneuvers the wheel forces are distributed optimally by prohibiting the five forms of fighting forces. By applying the control system to the nonlinear planar model and measuring the fighting forces, the controller also takes care of this effect when the wheels are not directed in a longitudinal direction. One can imagine the inner wheels of conventional cars steering under an enlarged angle which is enforced by the mechanical construction. The ATV shows the same behavior to prevent fighting forces during cornering using the nonlinear model.

In conclusion, a new allocation strategy is developed in this chapter. Normal

allocation techniques distribute control action among the inputs. When the distributed variable is not a system input but a system state, such as the tyre forces are no system inputs for the ATV, alternatives need to be tried out. Input transformation by servo loops are created to make the inputs approximately equal to the allocation variables. This transformation is sometimes difficult and always causes a difference between the inputs and the system states which have to be allocated. The newly developed strategy does not have problems with the allocation variables being system states instead of system inputs. Unallowed combination of the states which have to be allocated are created as new system outputs. This resulted in the case of the ATV as five forms of fighting tyre forces. By placing the plant including the additional outputs in a regular control loop, a high performance is obtained while the control action is optimally distributed.

Because of measurement difficulties, the controller is placed in a closed loop with the planar model, which approximates inverting the system up to a certain bandwidth. It is advantageous that no measurement data is required and the controller only requires a reference trajectory. Consequently, the disadvantage follows that it is impossible to compensate for system deviations, nor for disturbances.

Chapter 7

Controller design

The previous chapter showed the control structure in combination with the plant. The controller itself will be developed in this chapter.

7.1 $\mathcal{H}_2$ optimal control

Figure 6.5 of the previous chapter showed the control structure of the ATV. In that figure, the estimation model and plant were decoupled. For control design these models are assumed equal. Hence, the structure of figure 6.4 where these models are combined will be used.

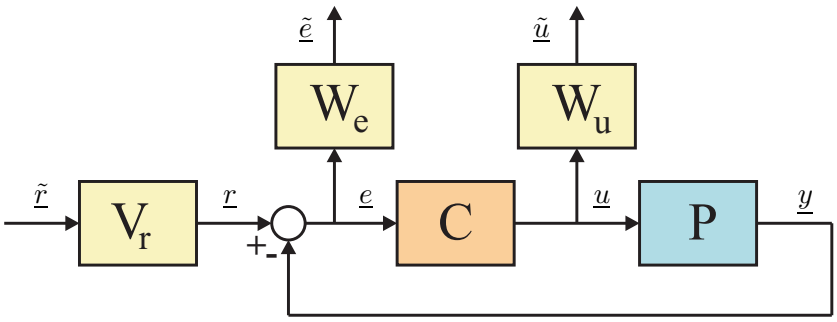

Figure 7.1: Control structure including filters

The augmented plant notation is used for control design. Outputs which are desired to be minimized are depicted in figure 7.1. Filters are added to

give a frequency weighing on both input and output signals. The weighed signals are denoted with a tilde.

The tracking error $\underline{\tilde{e}}$ needs to be minimized for good tracking and keeping the fighting tyre forces small. Added to the performance outputs are the control inputs to prevent actuator saturation, having a limited amount of differentiation for numerical computational speed and obtaining robustness. This structure is also called the mixed-sensitivity problem.

Another way of representing the scheme of figure 7.1 is by using the augmented plant G. The exogenous inputs are combined in the signal $\underline{\tilde{z}}$ and all control outputs are combined in $\underline{\tilde{z}}$.

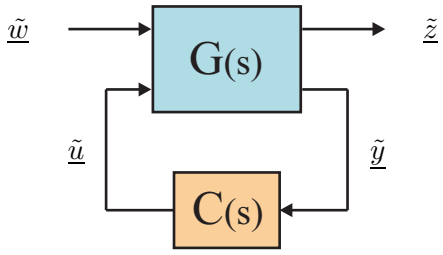

Figure 7.2: Augmented plant

Where the exogenous inputs and outputs equal the signals

$$\underline{\tilde{w}} = \underline{\tilde{r}} \quad and \quad \underline{\tilde{z}} = \begin{bmatrix} \underline{\tilde{e}} \\ \underline{\tilde{u}} \end{bmatrix} \tag{7.1}$$

And the augmented plant is defined as

$$G = \begin{bmatrix} W_e V_r & -W_e P \\ 0 & W_u \\ V_r & -P \end{bmatrix} \tag{7.2}$$

The choice between an energy optimal ($\mathcal{H}_2$, [20]) or maximum magnitude optimal controller ($\mathcal{H}_\infty$, [21] and [22]) is not trivial for this case. If requirements demand a minimal energy solution with know input spectra, $\mathcal{H}_2$ is preferred. When magnitude demands with known input specification on amplitude level exists, $\mathcal{H}_\infty$ gives the best solution. Mixed forms are also possible. Here, neither of the above demands applies where time delay up

to a certain frequency is the only performance demand. The availability of no clear reference specifications does not help in making this decision.

A $\mathcal{H}_2$ controller with sensitivity shaping approach is chosen. Filters are not based on demands of the actual signals, but on sensitivity and control sensitivity transfer function demands. Computational efforts of designing a $\mathcal{H}_2$ controller are relatively low. Further, minimal filter dynamics are preferred to obtain a low order controller. Magnitudes of independent signals such as control action are evaluated afterwards based on a possible trajectory.

The optimal controller will minimize the 2-norm of the transfer function from $\underline{\tilde{w}}$ to $\underline{\tilde{z}}$. This coincides with minimizing the energy of $\underline{\tilde{z}}$ for the case that unit power white noise is acting on exogenous input $\underline{\tilde{w}}$.

$$\min_{C} \left\| \begin{array}{c} W_e S V_r \\ W_u C S V_r \end{array} \right\|_2 \tag{7.3}$$

Where S is the sensitivity $\frac{1}{I+PC}$ and CS the control sensitivity $\frac{C}{I+PC}$.

7.2 Weighing filters

The weighing filters determine the final controller behavior. Tuning them properly is therefore an important task. Equation 7.3 shows that only the sensitivity and control sensitivity are minimized while there are three weighing filters available. This gives freedom in filter choice. In this case, the filter V_r is constant so that the tuning will only be performed with the filters W_e and W_u. As discussed before, tuning based on signal properties is not used in this case. The sensitivity and the control sensitivity are shaped in a specific way that will be explained in this section. All filters are depicted in figure 7.3.

The filter V_r is chosen to be a constant. This allows the possibility to tune with the other two filters and does not introduce additional states in the controller. Still, a variation in magnitude is given to show the relative difference in magnitude between the variables. The relative steady state values are used. The longitudinal and lateral speeds can vary approximately 5 m/s, while the yaw speed will not exceed 1 rad/s. Fighting forces will not be generated by a reference, but by differences between the model and reality. In this case, they are added to the reference as an external input. The amplitudes of the reference fighting forces are estimated not to exceed

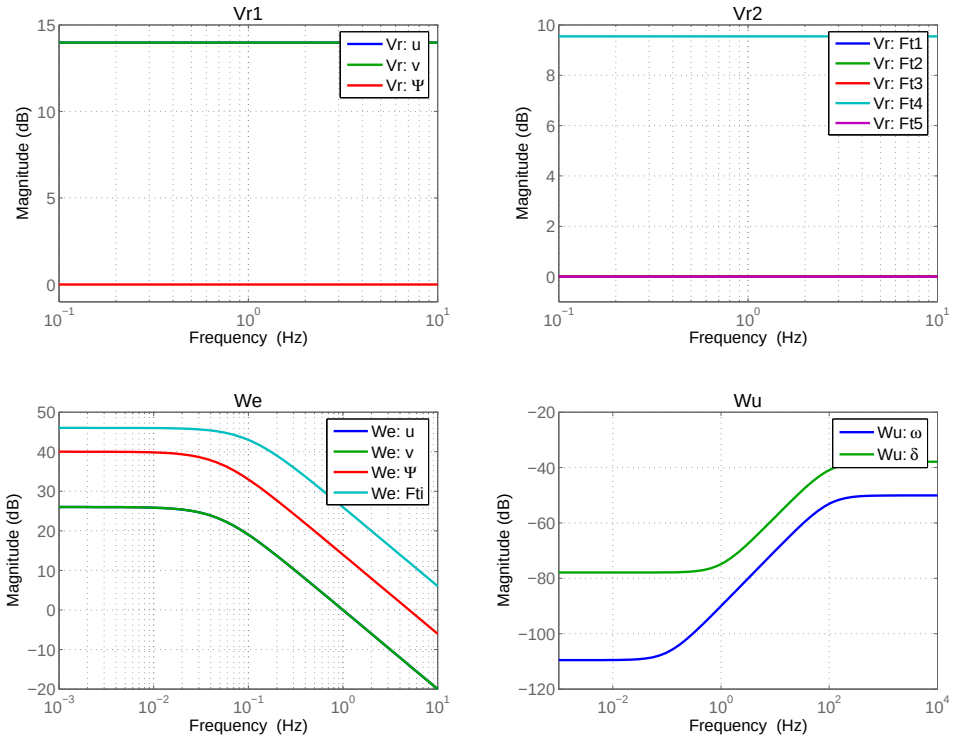

Figure 7.3: Tuning filters

a value of one. For the 4th fighting force, a value of three is chosen, because this is the main situation occurring during sharp cornering. At the maximum kinematic steering, the inner wheel angles are 45^o while the outer wheels steer at 18^o. This difference in angle during straight line driving is used to estimate this force.

W_e is tuned to obtain a desired sensitivity shape. The controller is designed such that it will minimize equation 7.3. At frequencies where the filters $W_e V_r$ have a high value, the sensitivity is forced to be low. The steady state error of the three velocities cannot allowed to be larger than 1% which states the sensitivity is required to be 0.01 at low frequencies. For the fighting tyre forces, a maximum allowed sensitivity of 0.005 is allowed. The bandwidth is slowly increased until satisfying results in time delay and gain errors for the velocities is obtained. A higher bandwidth is used for the fighting tyre forces.

The filters in W_u are lead filters with a cut-off frequency of 100 Hz. In this way they limit the control sensitivity at high frequencies. The controller

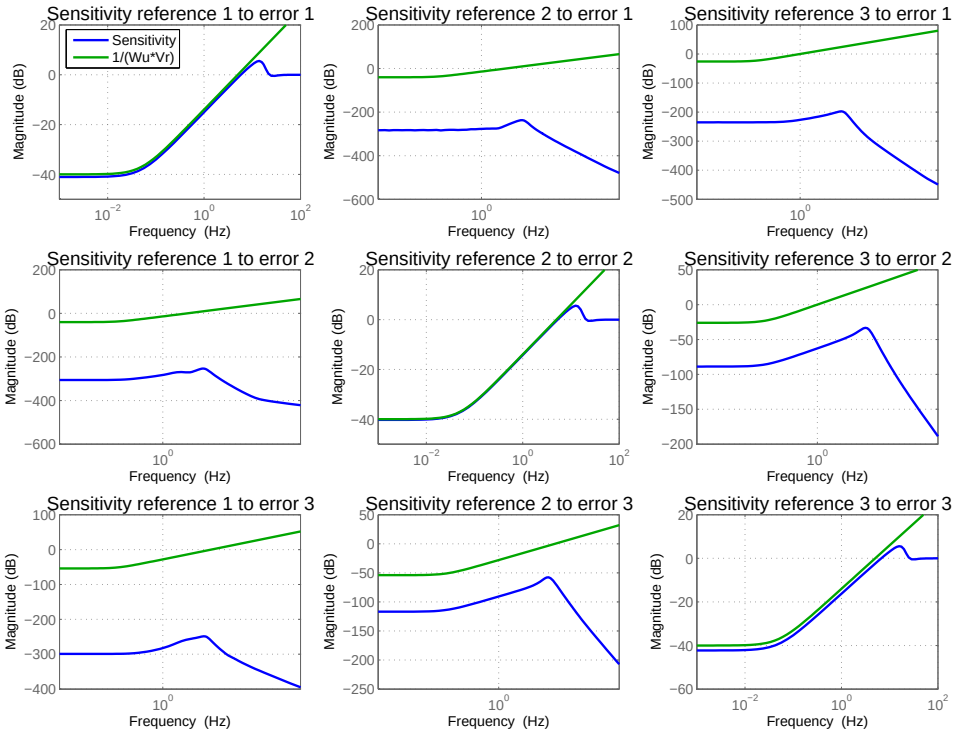

Figure 7.4: Required and real sensitivities

will only be allowed to have low frequent action. Relative differences between driving and steering actuators are again taken into account. The low frequent gain for driving is chosen as 1/20 which equals one divided by the maximum wheel speed variation. The maximum allowable acceleration is 20 rad/s^2 which gives a zero in the filter at one radian per second. The maximum steering angle is $\pi/4$ rad which gives the inverse magnitude of $W_{e,\delta}$ at low frequencies. The maximum steering velocity is $2 \cdot \pi$ rad/s with an accompanying zero at 8 rad/s. By pre-multiplying W_u with a constant, the complete control action will increase or decrease. Less controller restriction results in more freedom for shaping the sensitivity. The gain will be chosen such that the sensitivity lowers directly below the filters $W_e V_r$. Because of the constant reference over the frequency domain, the filter will not limit maximum actuator positions, but only limit control actions at high frequencies. Actuator saturation is dependent on the reference trajectory. After the tuning procedure, it is validated if actuator saturation occurs by means of simulation.

After a number of iteration steps, the final controller is found. It is imple-

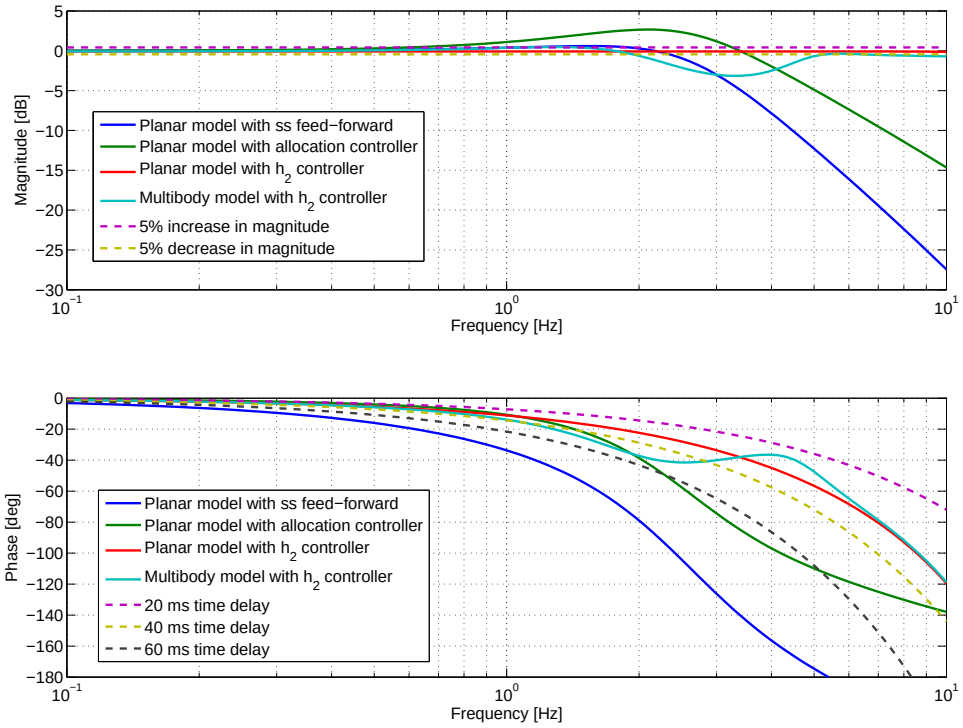

Figure 7.5: Bode diagram of $\frac{P_{planar}C}{I+P_{planar}C}_{(2,2)}$: from v_{ref} to v using $\mathcal{H}_2$ controller at a forward velocity of 5 m/s

mented as in figure 6.5. For figure 7.5, the linearized plant at a forward velocity of 5 m/s is used. Frequency responses show that the time delay of the system including $\mathcal{H}_2$ control is significantly reduced compared to the kinematic steering and allocation controller. Specifications are met when the controller is implemented on the planar plant. Reducing the time delay even more to meet the specifications for the multibody model is not considered useful, since experiments show that control effort and robustness decrease too much for good results. Pitch and roll effects cannot directly be manipulated by this controller and are not included in the controller model. If pitch and roll effects have to be reduced, constructional or active damping solutions are suggested.

More results of this controller are summarized in appendix I.

7.3 Switching control

The controller of the previous section is designed on the linearized planar model with a forward velocity of 5 m/s. According to this thesis' objectives, the controller has to function with forward velocities between 15 and 40 km/h. The influence of the non-linearitys can be seen in figure 7.6 where the controller tuned at 5 m/s is implemented at the ATV while driving 9 m/s. A resonance peak shows up between 10 and 20 Hz and causes undesired vibrations in the lateral direction at these frequencies during extreme maneuvers. An alternative controller is therefore required for this working area.

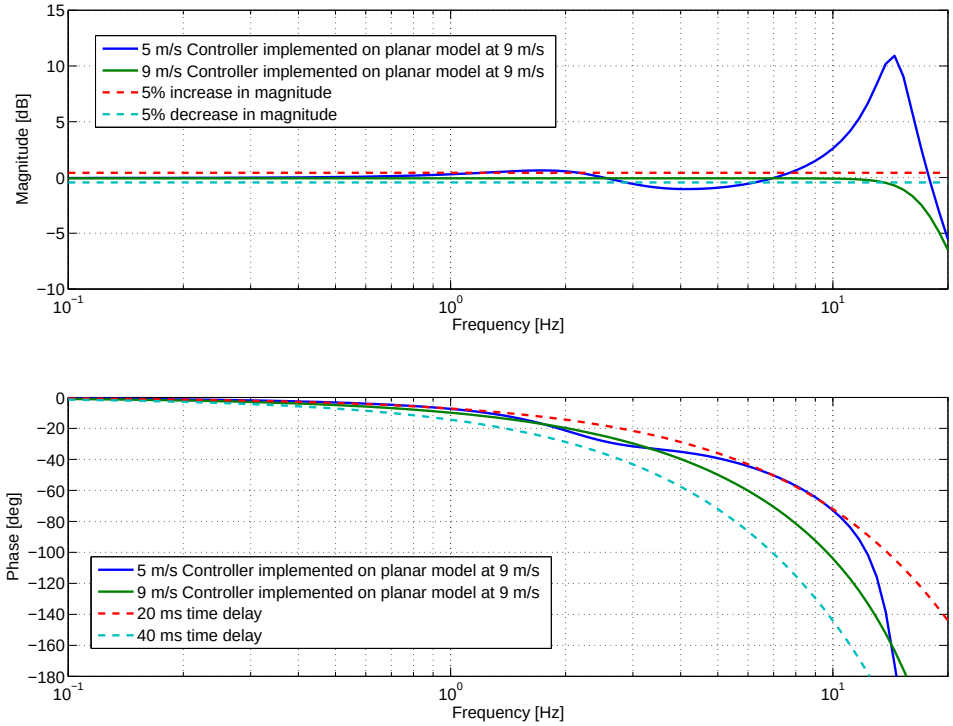

Figure 7.6: Bode diagram of $\frac{P_{planar}C}{I+P_{planar}C}{}_{(2,2)}$: from v_{ref} to v using $\mathcal{H}_2$ controller at a forward velocity of 9 m/s

Three controllers are designed at 5, 7 and 9 m/s. Identical weighing filters are used for each design as for the 5 m/s controller. Linear combinations of these controllers are connected to the model and weighed dependent on the forward velocity. Three half sinusoids are used for this weighing. The sum

of the three half sinusoids must always equal one [23]. In this way, the ideal controller for a certain forward velocity is approximated by interpolating the independent controllers as in figure 7.7.

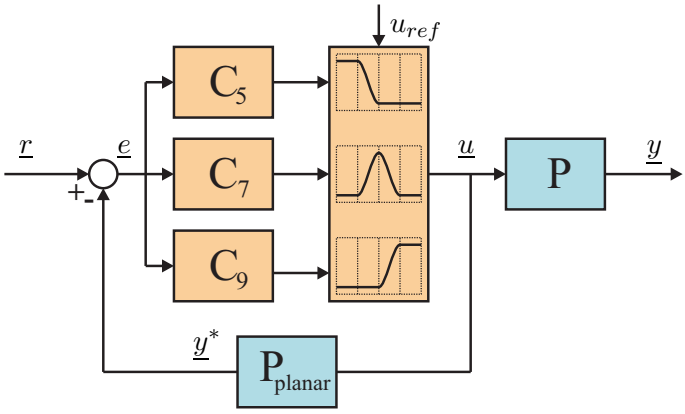

Figure 7.7: Switching control structure

No stability can be proven for this method. By the identical structures and the close working points of the controller and plants, it is plausible that the closed loop ATV system will be stable. Eigenvalues of multiple linear combinations of controllers applied to the model linearized at multiple forward speeds support this. In figure 7.8 the sensitivity is used as a stability margins indicator. A low maximum of the sensitivity does imply no major resonances and no closed loop poles near the imaginary axis. Linear combinations of the controller tuned at 5 m/s and 7 m/s are calculated and linear combinations of the controllers of 7 m/s and 9 m/s are calculated. These linear combinations of controllers are applied to the ATV planar model at different speeds. The ∞-norm of the 8×8 sensitivity is given as a function of these two variables.

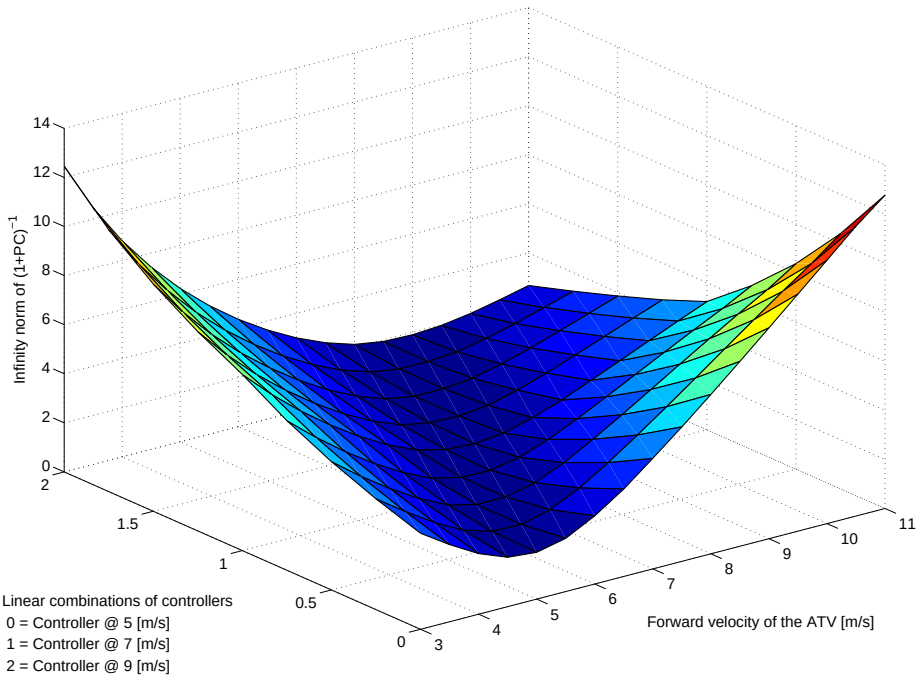

Figure 7.8: Sensitivity analysis for combinations of controllers and plants

7.4 $\mathcal{H}_\infty$ control

For $\mathcal{H}_2$ control it has already been mentioned that both a 2-norm minimization as an ∞-norm minimization would be suitable for the design of the ATV controller. Both methods are also explored in this thesis. In this section, a brief discussion is initiated about the advantages and disadvantages of using $\mathcal{H}_\infty$ control for the ATV.

During experimenting with both methods, almost identical performance is obtained. Because of the many uncertainties in reference specifications and no absolute error demands, the mixed sensitivity problem was very easy to tune using the $\mathcal{H}_2$ method.

When specific reference demands are available. $\mathcal{H}_\infty$ control becomes much more interesting. W_u can be modeled in a way to exactly represent the actuators. With the reference filter now generating realistic references and an error filter, this gives clear bounds on possible control actions. The

error filter remains difficult to model because of the relative performance demand, especially since minimal filter dynamics are desired to prevent the controller getting a higher order. A filter W_e with a frequency independent gain is preferable if low and high frequency demands can be represented approximately. A new filter V_n can be introduced to resemble non-existing measurement noise, cutting-off the controller at high frequencies. Constant values can be chosen for this filter so that no additional states are introduced in the controller. An additional advantage is that with the filter V_n, instead of a mixed-sensitivity problem a four block scheme is created and the algorithm will not simply use pole-zero cancellation according to Damen [21]. The system will acquire more performance robustness.

Performance or stability robustness cannot be proven for this system using $\mathcal{H}_\infty$ techniques. Because of the large non-linearity, the plant uncertainty would become too large for satisfying performance. Robust methods produce conservative controllers.

Chapter 8

Control system validation

The complete control system for the ATV has now been designed. Performance demands are formulated and achieved except for the differences caused by the pitch and roll dynamics. It is not considered reasonable to fully compensate for these dynamics with the current control structure.

During control design, a planar model with steady state tyres is used. In reality the ATV will pitch and roll when forces act on the vehicle during acceleration. Except that this causes diversions in acceleration at the center of gravity, this also causes load shifting of the vertical tyre forces. This will influence the horizontal tyre forces at constant slip rates. The nonlinear saturation of the tyres is another source of unpredicted reactions. Steering with the ATV is assessed in the time domain during the control design. The influences in the frequency domain have not been looked at before. In the beginning of this thesis, all these effects are assumed to not cause major problems. This premise will be validated in this chapter.

Because no real vehicle is present for validation, the realistic multibody model of chapter 4 is used. The most important masses are modeled independently in this model, and the non-linear dynamic MF-Tyre model is used for the tyres.

8.1 Reference trajectory

A reference trajectory has been developed by ADSE. Accelerations measured in a real car during the driving of a test track are scaled and filtered for a possible ATV trajectory. The driving velocity is lowered and the high frequencies are removed in this way. This trajectory is depicted in figure 8.1. The path of the controlled multibody model is also depicted and it follows the reference closely. Only slowly straying away the reference path was one of the requirements and has been met with this reference trajectory.

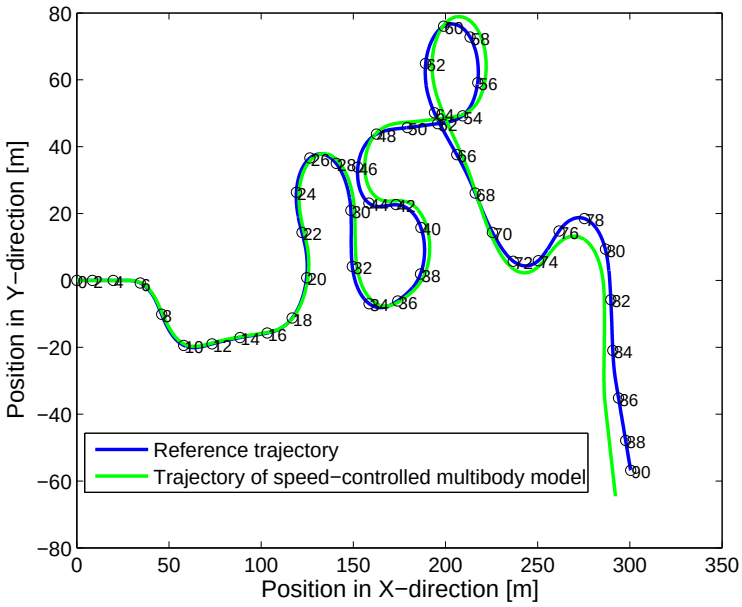

Figure 8.1: Trajectory of ATV

8.2 Performance

Figure 8.2 shows the reference and simulated accelerations in the three main directions, resulting in good tracking. On this scale, differences can hardly be seen.

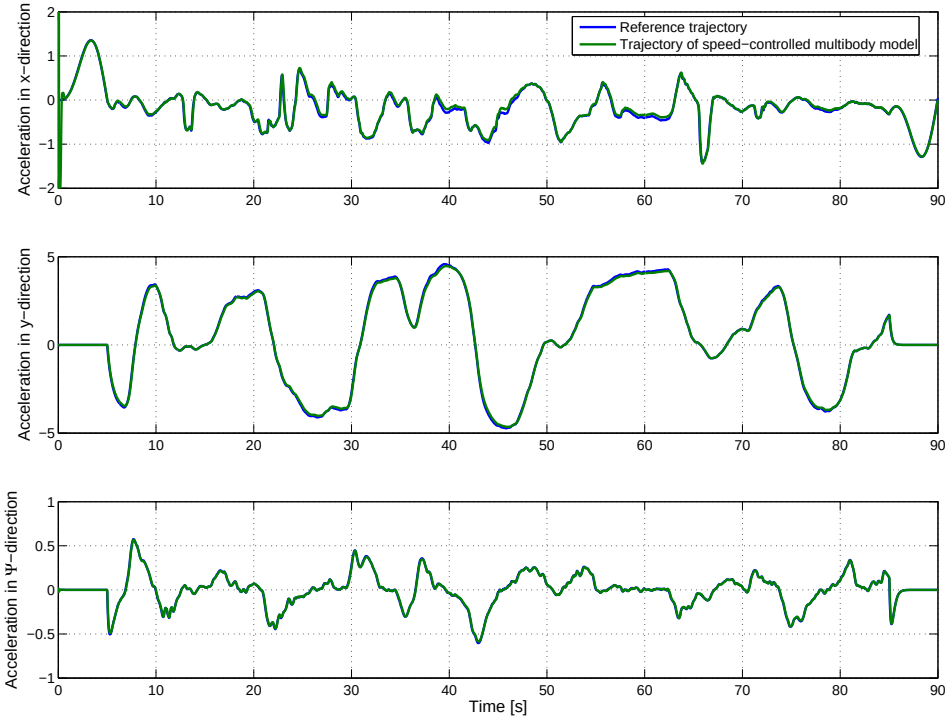

Figure 8.2: Step responses in three directions

Frequency responses are estimated based on the time domain data of figure 8.2. It is sampled at a frequency of 50 Hz and blocks of 512 samples or a length of 10.24 seconds are used. The blocks are large enough to capture a complete curve of the car and short enough to average several of them. Each block is filtered to reduce the effect of discrete steps at block intervals and averaged with overlap.

The coherence shows a good linear relation and the resulting frequency responses are as expected by the theoretical models. The lateral response can be compared with the frequency response of figure 7.5. The controller regulates the multibody model satisfying requirements.

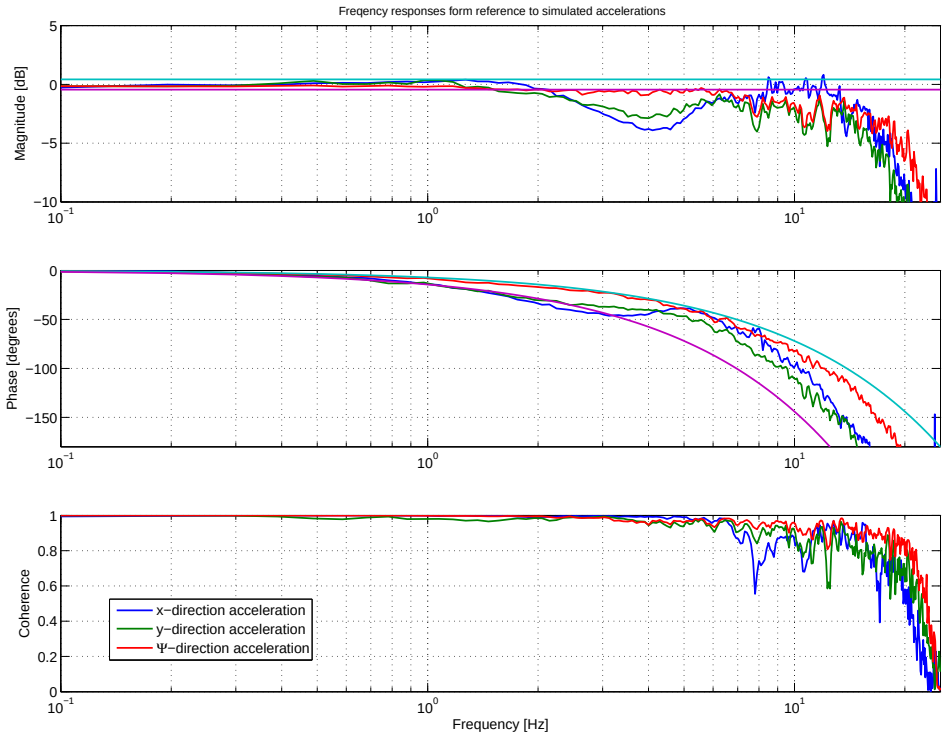

Figure 8.3: Measured frequency responses of $\frac{P_{multibody}C_{switching}}{I+P_{planar}C_{switching}}{}_{(1:3,1:3)}$: from reference velocities to real velocities using the switching $\mathcal{H}_2$ controller on the multibody model at a forward velocity ranging from 5 m/s - 9 m/s

8.3 Load sharing

Non-modeled load sharing is also investigated. In this thesis, the tyre forces were distributed such that they are distributed as equally as possible. During cornering, the vehicle will roll and the outer wheels will get a larger vertical load. This also makes these tyres capable of resisting larger horizontal loads. The controller steers the system in such a way every wheel gets the same absolute load.

In figure 8.4 the maximum relative tyre forces are divided by the average relative tyre forces and plotted for the ADSE test track. The green line shows the average relative tyre force. When the relative tyre forces become high, the difference between maximum the relative tyre force and the average relative tyre force is only 10%, which is a good result for the tyre force distribution. An explanation is that the controlled ATV distributes the tyre forces itself, by enforcing wheel angles and thereby actually wheel slip. With a constant slip the tyre will automatically produce a higher horizontal force with an higher vertical force.

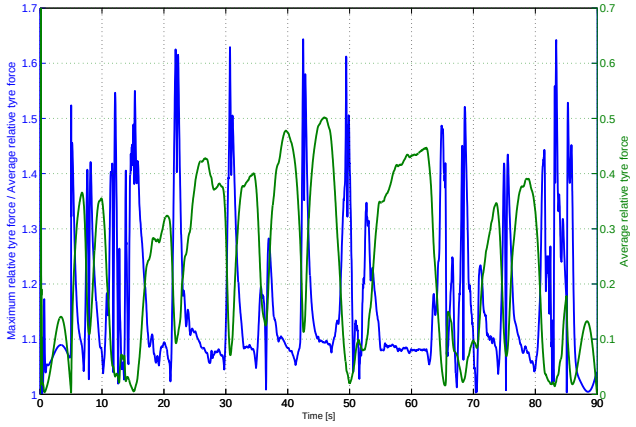

Figure 8.4: Relative tyre forces

Another interesting effect seen in the validation phase concerns the reference and control outputs. The reference trajectory originates from measurements of a normal car. A normal car can only steer with the front wheels which gives a coupling between lateral speed and yaw rate. After scaling and filtering the acceleration signals, this relation stays mostly intact. When looking at the control output, most of the steering action required appears to be done by the front wheels. This is purely caused by the trajectory accelera-

tion time history. Also the differential action normally accomplished by the rear differential in cars is taken care of in the controller. The inner wheels steer sharper than the outer wheels because of the smaller path radius. For this trajectory, the ATV emulates a car.

8.4 Tyre saturation

The previous reference trajectory contained accelerations up to 5 m/s^2. The nonlinear saturation region of the tyres was entered. Still, little effects of this saturation did return in the responses or result in performance degradation. A point of concern is the moment that uncontrolled slip will take place, the ATV will become uncontrollable which is a potentially dangerous situation.

Another trajectory developed by ADSE with higher acceleration is used for safety validation. A maximum acceleration of 7.9 m/s^2 is requested during this trajectory, this while the lateral friction coefficient μ_y is only 0.72. Theoretically, maximum accelerations of $\mu_y \cdot g = 7.1\ m/s^2$ are possible. Secondly the ATV has to corner over a radius so small the inner front wheel δ_1 has to steer at an angle of 1.05 radians while only $\pi/4 = 0.79$ radians are allowed. The construction, the controller and the tyres will be pushed over their limits. This situation is never allowed in reality and thus, this is a trajectory that will never be demanded. The reference acceleration demands and simulated acceleration are plotted in figure 8.5.

When pushed to the limit, figure 8.5 shows that the tyres of the ATV will saturate and a lower lateral acceleration is attained. The yaw velocity of the ATV is lower than the requested yaw velocity. In automotive terms, the ATV is under-steered for this maneuver. Why and if this is the case for other maneuvers is interesting for further research. There can be imagined that a wet or icy road may also introduce this phenomenon. During normal operation, the ATV is shown to be safe in ample margins.

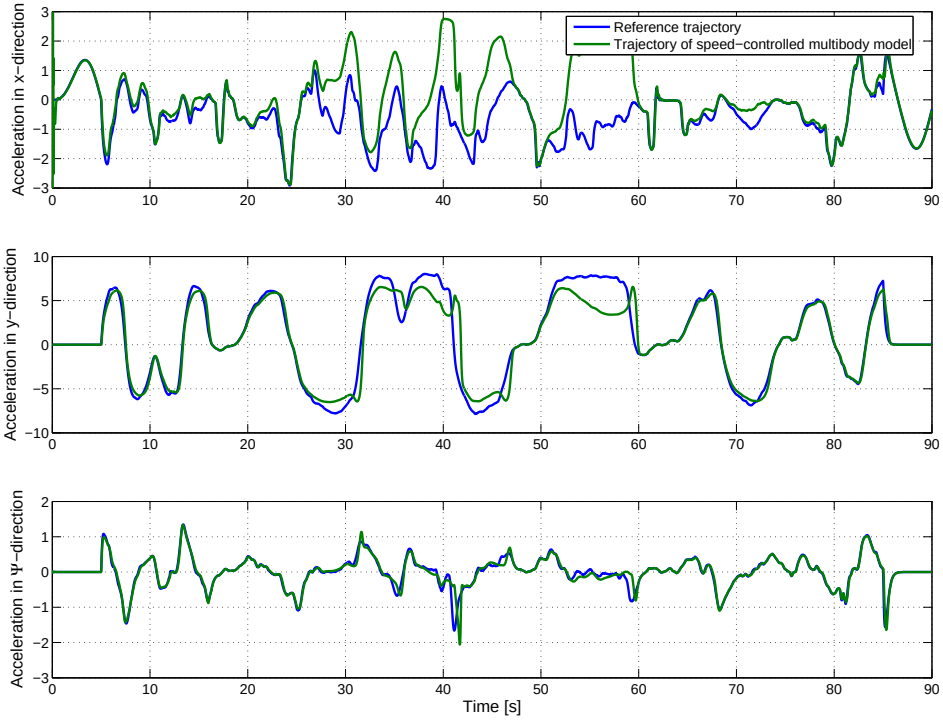

Figure 8.5: Reference and real accelerations during the test trajectory

Chapter 9

Conclusions, construction consequences and discussion

9.1 Conclusions

A control system for the four wheel driven and four wheel steered ADSE Test Vehicle has been designed for trajectories with speeds ranging from 15 to 40 km/h. Significantly faster responses than possible with current vehicle controllers are attained. The specified maximum time delay in acceleration of 40 ms for frequencies up to 2 Hz is mostly met. Close to 2 Hz, pitch and roll dynamics influence the system dynamics dominantly, which causes a time delay that slightly exceeds requirements. This is a constructional problem, which solution should not be tried to be found in adapting this controller. The controller compensates for tyre slip, tyre dynamics and actuator dynamics. Tyre forces are distributed optimally among all wheels for this overactuated vehicle.

A literature survey showed research has been done with quarter car models incorporating full dynamics or multi-wheeled models without tyre dynamics. The high actuation freedom and high performance demands require the combination of both strategies. A quarter-car model is made to obtain understanding of the basic dynamics of a vehicle. This model is extended to a planar model with four independently driven and steered wheels with full tyre dynamics. A validation model has also been produced in Matlab's multibody software Simmechanics. This model includes pitch, roll, advanced tyre dynamics and tyre saturation.

To distribute the control action over the different actuators of the over-actuated ATV, a new allocation strategy is developed. Classic solutions distribute control action with an allocation rule over the system's inputs. If the control action cannot directly be applied, a servo controller has to build this up as fast as possible causing unanticipated delays. The newly developed technique does not impose how control action has to be distributed, but what actuator combinations are not allowed to occur. Forbidden combinations of states are added as system outputs and are feedback controlled to be zero. This method is easy to implement and makes control up to high bandwidths possible.

In the validation phase there is checked for unmodeled effects such as load sharing and tyre saturation. Neither caused significant tracking errors. The ATV is proven not to get uncontrollable up to accelerations above the maximum allowed accelerations. The high performance and low response times obtained in the design phase is proven to last in the multibody simulations using frequency response measurements.

9.2 Construction design consequences

The design of this controller has a practical base because of the vehicle being developed by ADSE. Strong relations exist between the constructional design of the vehicle and the possible attainable performance of the controlled system. Hence, in this section, some comments are made upon both the controller and the vehicle design variables.

The most basic system dynamics result from the quarter car model which is explained in section 4.1. The calculated transfer functions clearly point out which design variables determine the system eigenfrequencies and damping. A high eigenfrequency shifts the phase lag to higher frequencies and makes the system controllable for high bandwidths. Well damped system properties are also preferred. Especially when eigenfrequencies shift in the frequency domain, as they velocity dependently do in the ATV case, resonance peaks can cause small stability margins.

To maximize the longitudinal and lateral eigenfrequencies positively, both tyre stiffnesses C_{fx} and C_{fy} should be high. A low vehicle mass m is desirable for lateral dynamics, while the longitudinal eigenfrequency will raise with a low wheel(motor) inertia divided by the squared effective radius J_w/r_e^2. The damping is in both cases mostly dependent on the tyre slip stiffnesses $C_{f\kappa}$ and $C_{f\alpha}$ and vehicle velocities, which need to be high.

Pitch and roll dynamics cause additional disturbances. The pitch/roll model of appendix E did not represent pitch and roll behavior well because of the large corner module masses. However it did show the parameters with a large influence. To reduce pitch and roll effects, the combined vertical tyre stiffness C_{fz} and suspension stiffness needs to be high. A low center of gravity, a low vehicle mass and high roll pole are also desired.

9.3 Discussion

This section is used to discuss some remaining issues related to this thesis.

The proposed controller is only suitable for the working range of velocities between 15 and 40 km/h. Outside this range, stability properties are not investigated thoroughly. When driving at negative speeds, the controlled system obviously becomes unstable. For slowly positioning the ATV without the demanded tracking performance, the simple kinematic steering of section 4.4 is proposed.

A very high performance is obtained with the used controller. Special vehicles, like the ATV, require this performance and a sophisticated controller with many states. Most autonomously guided vehicles however, will have acceptable performance with the allocated controller depicted in figure 5.4. The three allocation strategies of chapter 5 give help for a fast design procedure.

The newly developed allocation technique of section 6.1 creates interesting opportunities for other applications where actuator dynamics limit control bandwidth. By combining position and velocity outputs, it even seems possible to limit actuator rates by soft constraints. More research on this subject will be useful.

No thorough investigation of changing driving conditions such as changing slip stiffnesses due to tyre wear has been executed yet. Depending on the final driving environment this is advisable.

For future research is advised to start practical experiments first. Reality will show if the models describe the system well and if an additional feedback is necessary to compensate for model errors and disturbances in the open loop vehicle steering.

Bibliography

[1] Phileas; HOV-bus driving autonomously, Eindhoven, The Netherlands, http://www.phileas.nl

[2] TNO Automotive; Vehicle Hardware In the Loop Test Facility, Veldhoven, The Netherlands, http://www.automotive.tno.nl

[3] ADSE contact persons: S.K. Advani, G.J.C. Ransijn and W.H.J.J. van Staveren; ADSE, Saturnusstraat 12, 2132 HB Hoofddorp, The Netherlands; www.adse.nl

[4] Wolfgang Matschinksy; Road vehicle suspensions, Professional Engineering Publishing Limited, London, ISBN 1-86058-202-8, 2000

[5] Thomas. D. Gillespie; Fundamentals of vehicle dynamics, Society of Automotive Engineers, Inc, Warrendale, ISBN 1-56091-199-9, 1992

[6] Delft Tyre; Tyre models user manual, TNO Automotive, Delft, The Netherlands, May 2002

[7] Kiril Z. Rangelov; Simulink models of a quarter-vehicle with an antilock braking system, Stan Ackerman Institute, Mechatronic Design, Eindhoven, March 2004

[8] P.Khatun, C.M. Bingham, N. Schofield and P.H. Mellor; Application of fuzzy logic control algorithms for electric vehicle antilock braking/traction control systems, IEEE Transactions on vehicular technology, Vol 52, No 5, 2003

[9] Jürgen Ackermann, Jürgen Guldner, Wolfgang Sienel, Reinhold Steinhauser and Vadim I. Utkin; Linear and Nonlinear Controller Design for Robust Automatic Steering, IEEE transactions on control systems technology, Vol 3, No 1, 1995

[10] Kunsoo Huh and Joonyoung Kim; Active steering control based on the estimated tyre forces, Journal of Dynamic Systems, Measurement and Control, Vol 123, 2001

[11] Roel Leenen; Motion Control Design for a 4ws and 4wd overactuated vehicle, Master's Thesis, University of Technology Eindhoven, Department of mechanical engineering, Dynamics and control technology group, Eindhoven, DCT report nr. 2003.121, January 2004

[12] S.S. You and Y.H. Chai; Multi-Objective control synthesis: an application to 4WS passenger vehicles, Mechatronics, pp. 363-390, 1999

[13] I. Besselink; Vehicle dynamics, Lecture notes course 4L150, Eindhoven University of Technology, 2003

[14] The MathWorks, Inc; SimMechanics User's Guide, Natick, Massachusetts, http://www.mathworks.com/products/simmechanics/

[15] Hans B. Pacejka; Tyre and vehicle dynamics, Butterworth-Heinemann, Oxford, ISBN 0-7506-5141-5, 2002

[16] O. Härkegård; Backstepping and Control Allocation with Applications to Flight Control, Chapter 7, PhD. Thesis, Department of Electrical Engineering, Linkping University, Sweden, 2003

[17] Ram Venkataraman and David B. Doman; Control Allocation and Compensation for Over-Actuated Systems with Non-Linear Effectors, Proceedings of the American Control Conference, Arlington, VA June 25-27, 2001

[18] Panos Y. Papalambros and Douglass J. Wilde; Principles of Optimal Design: Modeling and Computation, Second edition, Cambridge University Press, Cambridge, ISBN 0-521-62727-3, 2000

[19] M.M.J. van de Wal; Selection of inputs and outputs for control, Technische Universiteit Eindhoven, Eindhoven, 1998, ISBN 90-386-0630-0

[20] Ali Saberi, Peddapullaiah Sannuti and Ben M. Chen; H_2 optimal control, Prentice Hall, Hertfordshire, 1995, ISBN 0-13-489752-X

[21] Ad Damen and Siep Weiland; Robust Control, Lecture notes for the class of robust control 5P430, University of Technology Eindhoven, Department of Electrical Engineering, Eindhoven, 2002

[22] Kemin Zhou; Essentials of Robus Control, International edition, Prentice Hall, Upper Saddle River, New Yersey, 1998, ISBN 0-13-790874-1

[23] Andrey V. Savkin and Robin J. Evans; Hybrid Dynamical Systems: Controller and sensor switching problems, Birkhäuser, Boston, 2002, ISBN 0-8176-4224-2

[24] Bram de Kraker and Dick H. van Campen; Mechanical vibrations, Lecture notes 4796, Eindhoven University of Technology, May 2003

[25] Nathan van de Wouw; Multibody dynamics, Lecture notes course 4J400, Eindhoven University of Technology, 2003

List of symbols

α Slip between tyre and road in lateral direction [−], page 99

α' Tyre contact patch lateral slip [−], page 104

ΔF_{pitch} Wheel load shift caused by pitch $[n]$, page 94

ΔF_{roll} Wheel load shift caused by roll $[n]$, page 94

δ_i Real steering angle $[rad]$, page 11

$\delta_{i,ref}$ Reference steering angle $[rad]$, page 13

γ Camber angle $[rad]$, page 99

κ Slip between tyre and road in longitudinal direction [−], page 99

κ' Tyre contact patch longitudinal slip [−], page 104

μ_x Longitudinal friction coefficient [−], page 9

μ_y Lateral friction coefficient [−], page 9

ω Rotational velocity of the wheel $[rad/s]$, page 13

ω_0 Omega where no longitudinal slip would occur $[rad/s]$, page 100

$\omega_{i,ref}$ Reference wheel speed $[rad/s]$, page 13

Ψ ATV rotation and rotation between world and ATV-fixed coordinate system, page 6

σ_α Lateral relaxation length $[m]$, page 105

σ_κ Longitudinal relaxation length $[m]$, page 105

$\sum F_x$ Total tyre force in ATV-fixed x-direction $[N]$, page 90

$\sum F_y$ Total tyre force in ATV-fixed y-direction $[N]$, page 90

$\sum M_z$ Total tyre torque in ATV-fixed z-direction $[Nm]$, page 90

τ_{hydr} Steering actuator time constant $[s]$, page 11

$\underline{q}$ Column of generalized coordinates, page 80

$\underline{Q}^{nc}$ Column of non-conservative generalized forces, page 80

$\underline{w}$ Exogenous control inputs, page 46

$\underline{z}$ Performance outputs to be controlled, page 46

A State space dynamics matrix A, page 81

a Half the axle base $[m]$, page 6

B State space input matrix B, page 81

C Feedback controller of dimensions 8×8, page 41

C State space output matrix C, page 81

C_ω Gain of driving servo controller $[Nms/rad]$, page 13

$C_{f\alpha}$ Vertical slip stiffness $[Ns/m]$, page 9

$C_{f\kappa}$ Longitudinal slip stiffness $[Ns/m]$, page 9

C_{fx} Longitudinal carcass stiffness $[N/m]$, page 9

C_{fy} Lateral carcass stiffness $[N/m]$, page 9

C_{fz} Vertical carcass stiffness $[N/m]$, page 9

CS Control sensitivity $\frac{C}{I+PC}$, page 47

D Damping matrix in Lagrange equations of motion, page 80

D State space input feed-through matrix D, page 81

D_{fz} Vertical damping $[Ns/m]$, page 9

F Feed-forward allocation controller of dimensions 8×3, page 33

F_{cmx} Tyre force in ATV-fixed x-direction $[N]$, page 23

F_{cmy} Tyre force in ATV-fixed y-direction $[N]$, page 23

F_{cpx} Tyre contact patch force in wheelcarrier-fixed x-direction $[N]$, page 107

F_{cpy} Tyre contact patch force in wheelcarrier-fixed y-direction $[N]$, page 107

F_{tf} Dimensionless fighting tyre force [-], page 39

F_{tx} Tyre force in wheelcarrier-fixed x-direction $[N]$, page 99

F_{ty} Tyre force in wheelcarrier-fixed y-direction$[N]$, page 99

F_{tzN} Nominal tyre load [N], page 101

F_{tz} Vertical wheel load $[N]$, page 94

F_{zN} Nominal vertical tyre load [N], page 39

G Augmented plant, page 46

H Servo controlled 3×8 ATV plant with velocity outputs, page 13

h Height to center of gravity $[m]$, page 7

I Inertia $[kg/m^2]$, page 7

K Stiffness matrix in Lagrange equations of motion, page 80

M Mass matrix in Lagrange equations of motion, page 80

m Mass $[kg]$, page 7

P Servo controlled 8×8 ATV plant including fighting forces outputs, page 39

Q Control allocation transformation of size 8×3, page 30

R Kinematic steering matrix of dimensions 8×3, page 25

R_b Radius of main body $[m]$, page 6

r_e Effective rolling radius $[m]$, page 100

S Sensitivity $\frac{1}{I+PC}$, page 47

s Half the track width $[m]$, page 6

T Total kinetic energy of system, page 80

T_m Motor torque $[Nm]$, page 11

u Longitudinal velocity at the platform CG $[m/s]$, page 6

u_t Longitudinal tyre carcass deflection $[m]$, page 104

V Total potential energy of system, page 80

v Lateral velocity at the platform CG $[m/s]$, page 6

v_t Lateral tyre carcass deflection $[m]$, page 104

V_x Longitudinal velocity of the wheel in wheelcarrier-fixed coordinates $[m/s]$, page 100

V_{sx} Longitudinal slip velocity of the wheel in wheelcarrier-fixed coordinates $[m/s]$, page 100

V_{sy} Lateral slip velocity of the wheel in wheelcarrier-fixed coordinates $[m/s]$, page 100

X World-fixed ATV x-coordinate, page 6

x ATV-fixed ATV x-coordinate, page 6

Y World-fixed ATV y-coordinate, page 6

y ATV-fixed ATV y-coordinate, page 6

$V_{sx}{}'$ Longitudinal slip velocity of contact patch $[m/s]$, page 104

$V_{sy}{}'$ Lateral slip velocity of contact patch $[m/s]$, page 104

4WD Four Wheel Driven, page 2

4WS Four Wheel Steered, page 2

ADSE Aircraft Development and Systems Engineering B.V, Hoofddorp, page 2

ATV ADSE Test Vehicle, page 2

CM Corner Module: wheel + wheel carrier + suspension system, page 7

COG Center of Gravity, page 6

RP Roll Pole, page 8

Appendix A

ATV control system requirements

The objectives of the control design are stated in chapter 1. In this appendix, the full ATV control system requirements are listed.

Performance requirements:

- A maximum time delay of 20 ms between reference and real acceleration in the COG is aspired. This corresponds with a phase revolution of 14.4^o at 2 Hz.
- A time delay of 40 ms between reference and real acceleration in the COG up to 2 Hz is maximally allowed. This corresponds with a phase revolution of 28.8^o at 2 Hz.
- Maximum allowed acceleration gain errors of 5% for frequencies up to 2 Hz (12.6 rad/s) are allowed.
- The amount of parasitic accelerations directly produced by actuators or indirectly through suspension in pitch and roll direction must be minimal.

Constraints:

- Operating the ATV must be safe in all possible scenarios for velocities between 15 and 40 km/h.

- Wheels can maximally steer up to an angle of 45^o.
- Uncontrolled slip has to be prevented within all driving conditions.

Other requirements:

- Minimal power usage of actuators is desired.
- Minimal amount of sound production is desired.

Appendix B

Assumptions summary

- All bodies are assumed rigid. Deformations only occurs at predefined locations such as the suspension system and tyres according to the linear relations between force and position or velocity.
- The time delay of the electrical system of the driving motors is negligible. The motors are linear in their working range.
- The hydraulic system actuates on velocity level with negligible dynamics and can produce unlimited forces.
- The MF-Tyre model resembles reality and all tyre parameters are known. Four identical tyres are used on the ATV.
- The mass of the ATV is distributed equally over the vehicle. The COG is located in the geometrical center of the ATV and the mass distribution is as modeled in the multibody model.
- Different assumptions are used for the different models. Unmodeled and modeled properties are summarized in table 4.1.
- The tyre forces are assumed approximately equal in wheelcarrier reference frame and ATV-fixed coordinates for the definition of fighting forces.

Appendix C

Vertical model

In section 2.2, the suspension system of the ATV is discussed. The conclusion is that pitch, roll and other parasitic movements never can be fully avoided. It is essential that oscillations damp out quickly to obtain a smooth ride. For this purpose, in this appendix, the optimal values for suspension stiffness and damping are found in a structural way. A model has been made to investigate the vertical dynamics including small pitch and roll movements of the platform. A scheme of the system is depicted in figure C.1.

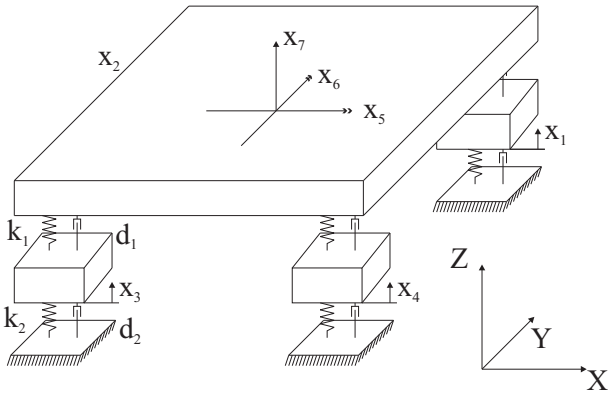

Figure C.1: Scheme of vertical model

For this system, masses and moments of inertias are known and summed up in previous sections. The spring stiffness of the tyres k_2 is $1 \cdot 10^6$ $[N/m]$. The small internal damping of the tyres d_2 is 500 $[Ns/m]$. A suspension system has to be designed to improve overall damping behavior. The model

gives insight to choose suitable parameters for the suspension stiffness k_1 and damping d_1. The system equations have been modeled using the Lagrange equations of motion modeling [24]. The next generalized coordinates are used:

$$\underline{q} = [\ x_1 \quad x_2 \quad x_3 \quad x_4 \quad x_5 \quad x_6 \quad x_7\ ]^T \tag{C.1}$$

The total kinetic energy of the system equals

$$T = \frac{1}{2}m_2(\dot{x}_1^2 + \dot{x}_2^2 + \dot{x}_3^2 + \dot{x}_4^2) + \frac{1}{2}m_1\dot{x}_7^2 + \frac{1}{2}J(\dot{x}_5^2 + \dot{x}_6^2) \tag{C.2}$$

With the coordinates x_i defines as in figure C.1. The total potential energy of the system is

$$\begin{aligned} V = \frac{1}{2}k_1[&(x_1 - sx_5 + ax_6 - x_7)^2 + (x_2 - sx_5 - ax_6 - x_7)^2 \\ &+(x_3 + sx_5 - ax_6 - x_7)^2 + (x_4 + sx_5 + ax_6 - x_7)^2] \\ &+\frac{1}{2}k_2(x_1^2 + x_2^2 + x_3^2 + x_4^2) \end{aligned} \tag{C.3}$$

With non-conservative generalized forces of

$$\underline{Q}^{nc} = \begin{bmatrix} -d_2\dot{x}_1 - d_2(\dot{x}_1 - s\dot{x}_5 + a\dot{x}_6 - \dot{x}_7) \\ -d_2\dot{x}_2 - d_2(\dot{x}_2 - s\dot{x}_5 - a\dot{x}_6 - \dot{x}_7) \\ -d_2\dot{x}_3 - d_2(\dot{x}_3 + s\dot{x}_5 - a\dot{x}_6 - \dot{x}_7) \\ -d_2\dot{x}_4 - d_2(\dot{x}_4 + s\dot{x}_5 + a\dot{x}_6 - \dot{x}_7) \\ d_2s(\dot{x}_1 + \dot{x}_2 - \dot{x}_3 - \dot{x}_4) - 4d_2s^2\dot{x}_5 \\ d_2a(-\dot{x}_1 + \dot{x}_2 + \dot{x}_3 - \dot{x}_4) - 4d_2a^2\dot{x}_6 \\ d_2(x_1 + x_2 + x_3 + x_4 - 4x_7) \end{bmatrix} \tag{C.4}$$

The Lagrange equations of motion can now be used

$$\frac{d}{dt}(T_{,\underline{\dot{q}}}) - T_{,\underline{q}} + V_{,\underline{q}} = (\underline{Q}^{nc})^T \tag{C.5}$$

In the linearized case, the following linear equation can be derived

$$M\underline{\ddot{q}}(t) + D\underline{\dot{q}}(t) + K\underline{q}(t) = Q(t) \tag{C.6}$$

where M is the mass matrix, D the damping matrix and K the stiffness matrix. Q define the input signals. These matrices can be derived in the following way

$$\begin{aligned} \frac{d}{dt}(T_{,\underline{\dot{q}}}) &= \underline{\dot{m}} + M\underline{\dot{q}} && \text{(C.7)} \\ T_{,\underline{q}} &= \underline{0} && \text{(C.8)} \\ V_{,\underline{q}} &= \underline{k} + Kq && \text{(C.9)} \\ (\underline{Q}^{nc})^T &= \underline{f}(t) - D\underline{\dot{q}} && \text{(C.10)} \\ Q(t) &= -\underline{\dot{m}}(t) - \underline{k}(t) + \underline{f}(t) && \text{(C.11)} \end{aligned}$$

The above linear Lagrange equation is of second order. For analysis, first order equations are desired to determine the poles of the system. Therefore, the system is converted to the first order state-space notation

$$\dot{\underline{x}}(t) = A\underline{x}(t) + Bu(t) \tag{C.12}$$

with the new state

$$\underline{x} = \begin{bmatrix} \underline{q} \\ \dot{\underline{q}} \end{bmatrix} \tag{C.13}$$

and matrices

$$A = \begin{bmatrix} \underline{0} & \underline{I} \\ -M^{-1}K & M^{-1}D \end{bmatrix}, \qquad B\underline{u}(t) = \begin{bmatrix} \underline{0} \\ M^{-1}Q(t) \end{bmatrix} \tag{C.14}$$

Now, the eigenvalue problem for systems with general damping and symmetric matrices can be solved.

$$(sI - A)\underline{v} = \underline{0} \tag{C.15}$$

the poles s of the system are determined by

$$det(sI - A) = 0 \tag{C.16}$$

Using the above procedure, the dynamic equations, the eigenvalues and the eigenmodes of the system are derived. The goal of this exercise was to find suitable parameters for suspension stiffness and damping such that the pitch and roll models will be well dampened. How well an eigenmode is damped is determined by the ratio of the real and imaginary parts of the eigenvalues belonging to that eigenmode. A large negative real part coincides with a good damping.

Generally, five different eigenmodes can be distinguished. In the first eigenmode, the whole platform moves vertically up and down while the unsprung masses move in phase with the platform. When the unsprung mass would be fixated on the platform, the undamped frequency of this mode would be 21 [rad/s]. The second eigenmode is a mode in which the platform is pitching or rolling. The unsprung masses, again move in phase with the platform. The eigenfrequencies for pitch and roll are identical since masses and lengths are identical. When the unsprung mass would be fixated on the platform, the undamped frequency of this mode would be 28 [rad/s]. The third eigenmode is similar as the first one, with exception that the unsprung masses now move in anti-phase. The relatively lightweight unsprung masses are moving heavily while the platform itself moves much less. This

phenomenon is called wheel-hop and occurs mostly at high frequencies. The fourth eigenmode is again a pitch/roll mode like the second one. Here again, the platform and the unsprung masses are moving in anti-phase which is another form of wheel hop. In the fifth mode, wheels on the one diagonal move up, while wheels on the other diagonal move down, in this form of wheel hop, the main platform is force balanced and does not move at all. These five eigenmodes are depicted in figure C.2.

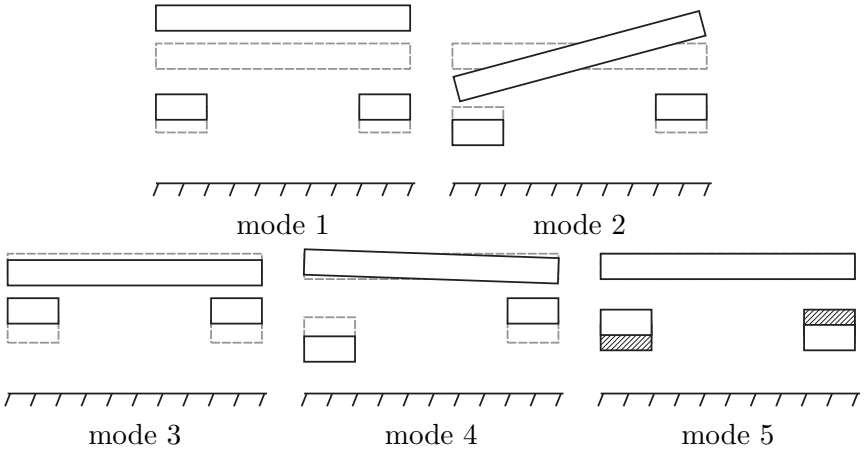

Figure C.2: Eigenmodes of vertical model

In figure C.3, the real and imaginary part of the system poles are plotted for different values of suspension stiffness k_1 and damping d_1. The different colors signify a different suspension stiffness. The curves, made of closely spaced dots are poles with slowly changing suspension damping. Damping is varied form 0 to 50,000 [Ns/m] in steps of 100 [Ns/m].

Looking at figure C.3, the five eigenfrequencies can be distinguished. Also, looking at the imaginary axis, the poles for zero damping can be found. Notice, that with lower suspension stiffness, undamped eigenfrequencies will move down. When the damping will be increased up to unrealistic high values, again, a fixed connection between platform and unsprung mass is created. The eigenvalues relating to the first and second eigenmodes will move back to the original undamped eigenfrequencies of 21 and 28 [rad/s], while the wheel hop modes completely disappear on the real axis. An interesting change of polar orbits can be noticed between the red and green curves. This is caused because there is no Rayleigh damping in this model, only general damping applies [24].

Blue dots	Suspension stiffness 500,000 [N/m]
Red dots	Suspension stiffness 250,000 [N/m]
Green dots	Suspension stiffness 166,667 [N/m]
Magenta dots	Suspension stiffness 125,000 [N/m]

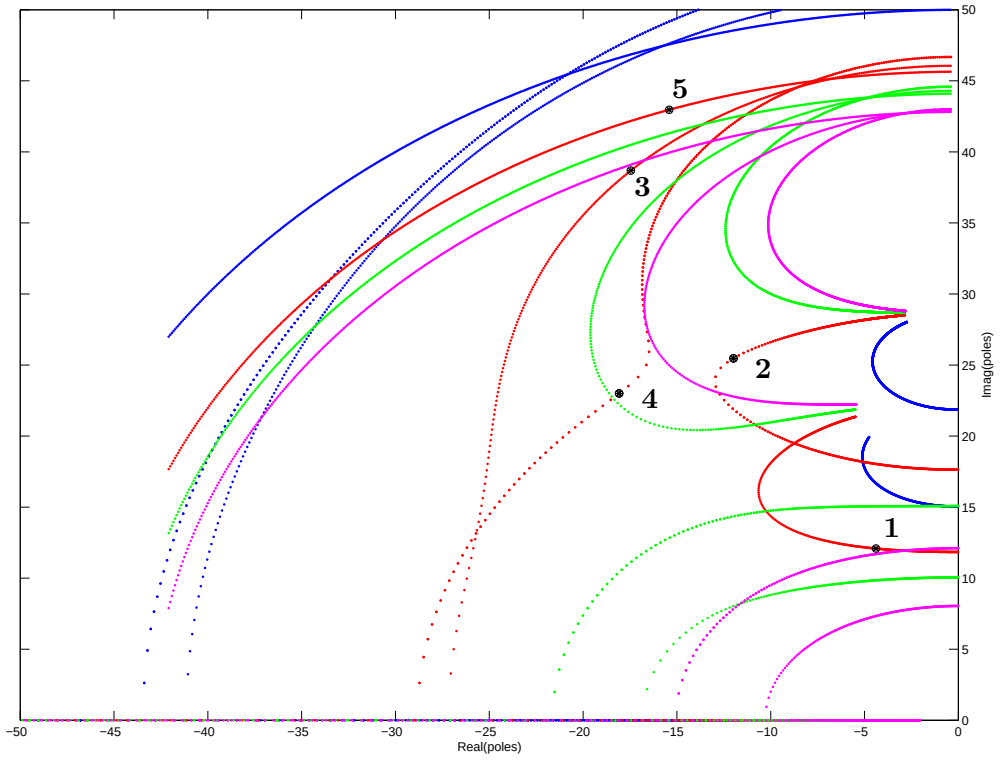

Figure C.3: Pole lines of the vertical model

Optimal suspension parameters can be chosen. Special attention is paid to eigenmode two, since this eigenmode will be mostly excited by acceleration and cornering. The eigenvalue belonging to this mode has to have a real part which is as big as possible for good damping while the frequency of the eigenmode is not decreased too much. Choosing the optimal suspension parameters is done based on the above criterium by looking at figure C.3. The optimal suspension parameters are a spring stiffness of 250,000 [N/m] and damper constant of 18,000 [Ns/m]. Poles belonging to this parameter setting are marked black in figure C.3.

Appendix D

Servo-control for wheelspeed

In section 2.5, a wheel speed servo-controller is proposed. The controller has to make the wheel driving at reference speed. Therefore the velocity of the wheel is measured and fed back. The controller compares the reference and real speed and multiplies this error with a single gain. This is the driving torque the wheel motor has to produce. In this section, the stability of this controller will be handled based on a quarter car model. The equations of motion used in this model and used symbols can be looked up in chapter 4.

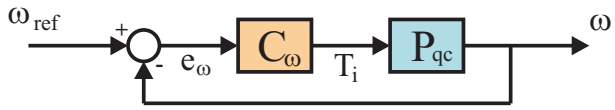

Figure D.1: Control scheme for servo control

A dynamic model of a quarter car is made. There is no interaction between the wheels and no load shifting assumed. In figure D.2, the different inertias of the quarter-car model are decomposed for a Newton-Euler equations of motion approach. At each decomposition, equilibrium of forces exists.

The belonging equations of motion are

$$m_{total}\dot{u} = F_{tx} \tag{D.1}$$

$$J_w\dot{\omega} = -r_e \cdot F_{tx} + T \tag{D.2}$$

$$\dot{u_t} + \frac{C_{fx}}{C_{f\kappa}}|u|u_t = r_e\omega - V_x \tag{D.3}$$

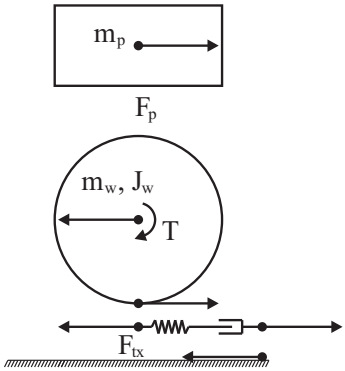

Figure D.2: Decomposed quarter-car model

where

$$F_{tx} = C_{fx} u_t \tag{D.4}$$

The equations of motion are linearized around the equilibrium of a forward velocity u of 5 m/s. A summed mass of the wheel and platform m_{total} of 2000 kg is used. The inertia of the wheel Jw is estimated at 115 $kg\ m^2$. This because of the added inertia of the motor which is connected through a gearbox with a reduction factor 6. The torque T is the demanded torque at the wheel, the torque at the motor will be a factor 6 lower. The bode response from input torque T to wheel speed ω is depicted in figure D.3.

A servo-controller with a single gain of 11,000 Ns/m is chosen. This is identical with a controller gain of 81 dB. Hence, the open loop bode diagram will rise 81 dB. The phase at the highest cross-over frequency of the open-loop will be less then 90^o delayed at an frequency of about 20 Hz. According to the nyquist criterion, a stable closed loop system is obtained. A bandwidth of 20 Hz is quite high for system with such a high inertia. Especially the gearbox will introduce a low stiffness not taken along in this model. One has to be attentive for stability problems if the wheel speed is going to be measured after the gearbox.

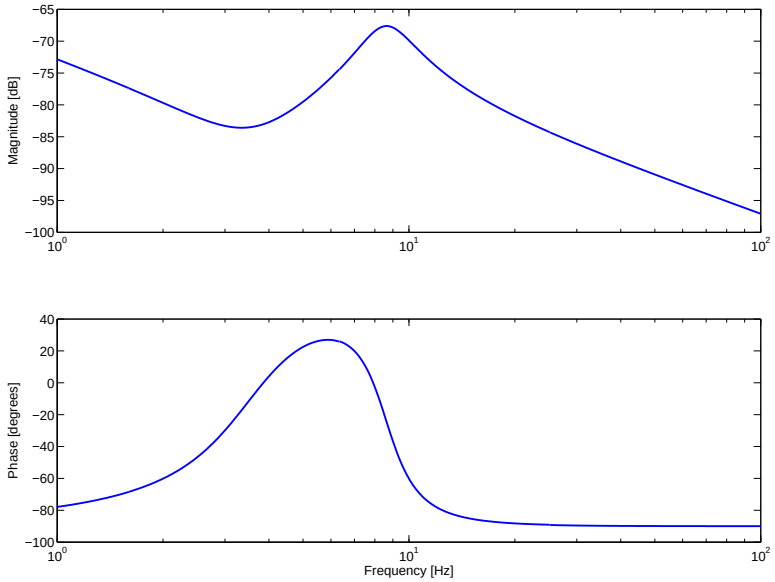

Figure D.3: Bodeplot of lateral open-loop system

Appendix E

Dynamical models of the ATV construction

Planar model

The simplest model of the ATV construction is a mass moving with three degrees of freedom in the horizontal plane as depicted in figure E.1. The world coordinates are named with uppercase letters X and Y, while in ATV-fixed coordinates is referred to as x and y in lowercase letters. The rotational degree of freedom Ψ is not dependent on world or ATV-fixed coordinates. This definition will be used from now on.

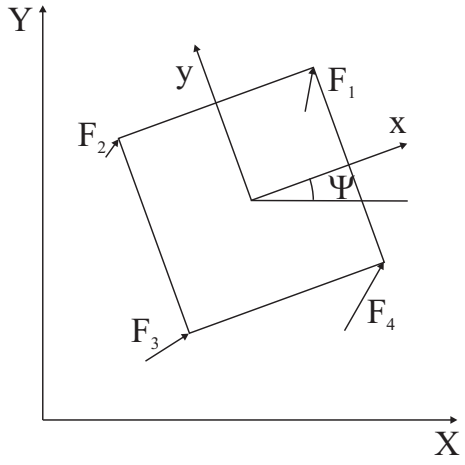

Figure E.1: Scheme of ATV planar model

The equations of motion for this system are derived with the Newton-Euler equations of motion. Expressed in the global coordinates, the equations of motion are straightforward. Here, they are expressed in a more meaningful body-fixed coordinate system.

$$\begin{aligned} \dot{u} = &\quad v\dot{\Psi} + \frac{1}{m}\sum F_x \\ \dot{v} = &-u\dot{\Psi} + \frac{1}{m}\sum F_y \\ \ddot{\Psi} = &\quad \frac{1}{J_z}\sum M_z \end{aligned} \tag{E.1}$$

With u the forward velocity, v the lateral velocity, m the total construction mass and J_z the inertia around the z-axis. The sum of forces and the sum of torques are composed of the individual corner module forces and equal:

$$\begin{aligned} \sum F_x &= \sum_{i=1}^{4} F_{cmxi} \\ \sum F_y &= \sum_{i=1}^{4} F_{cmyi} \\ \sum M_z &= s(-F_{cmx1} - F_{cmx2} + F_{cmx3} + F_{cmx4}) \ldots \\ &\quad + a(F_{cmy1} - F_{cmy2} - F_{cmy3} + F_{cmy4}) \end{aligned} \tag{E.2}$$

By choosing the representation in the body-fixed coordinate system, even for this simple model, nonlinear equations are obtained as can been seen in equation E.1. Using the local platform axis system is more useful since the driver is sitting on that platform. The wheels are also mounted on the platform and steered relatively to the platform. The driver will experience the accelerations in the center of gravity as:

$$\begin{aligned} a_x = &-v\dot{\Psi} + \dot{u} = &\quad \frac{1}{m}\sum F_x \\ a_y = &\quad u\dot{\Psi} + \dot{v} = &\quad \frac{1}{m}\sum F_y \\ a_\Psi = &\quad \ddot{\Psi} = &\quad \frac{1}{J_z}\sum M_z \end{aligned} \tag{E.3}$$

Pitch/Roll model

The planar model is the simplest model for analyzing the dynamics of the ATV main body. In reality, forces do not affect the main body in the horizontal plane through the COG. The forces affect the body on floor level which generates pitch and roll torques around the COG. The suspension takes care of resistance moments and stability. The rolling and pitching will generate a difference between wheel speeds and the speed of the center of gravity. Since the input signals are acting on the wheels and the outputs are the COG accelerations, the influences of these effects have to be examined.

A simple model where roll is included around the roll-axis that is used in references [5] and [13] is depicted in figure E.2. This model only allows roll around the roll-axis as explained in section 2.2. The construction below the roll-axis is assumed massless and stiff. It will react instantly. When a force $\sum F_y$ is applied at the tyres, this horizontal force will be equivalent to the horizontal force along the roll-axis. Additionally, there is a torque produced in the roll-axis by the spring-damper system which represents the suspension of the vehicle. These forces and torques react over an arm with the inertia. By making static equilibrium of torques and forces of the lower part the vertical load shifting of the tyre forces is defined.

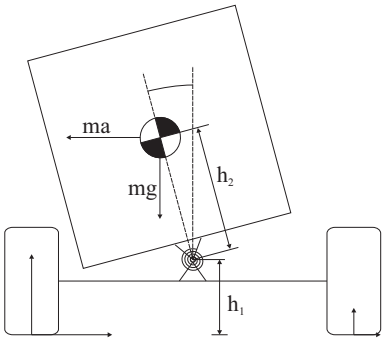

Figure E.2: Scheme of roll model

The ATV will undergo large longitudinal and lateral accelerations. Also, the suspension system is designed in such a way that both anti-roll and anti-pitch are obtained. The roll-axis is placed horizontal in the longitudinal direction of the vehicle. Because of the symmetry of the construction, a similar pitch-axis can be imagined in the horizontal plane perpendicular tot the roll-axis. Combining these axes, would result in rotation around one roll/pitch-pole.

The equations of motion for this model will be derived with the Newton Euler equations. Because of the high number of rotational transformations present, a systematic approach is used for coordinate transformations in order to acquire the equations of motion [25]. The different coordinate systems and model structure is depicted in figure E.3.

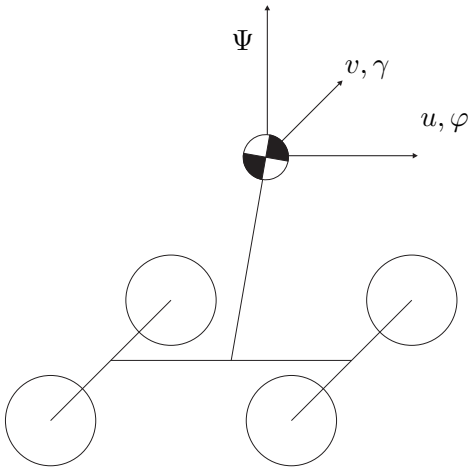

Figure E.3: Scheme of pitch/roll model

Coordinates systems used for equations are the world-fixed coordinate system $\underline{\vec{e}}^0$, the base-fixed coordinate system $\underline{\vec{e}}^1$ and the rolling and pitching coordinate system $\underline{\vec{e}}^2$. Used coordinates are longitudinal velocity u, lateral velocity v, pitch angle γ, roll angle φ and yaw velocity $\dot{\Psi}$ which are all represented in $\underline{\vec{e}}^1$. The mass of this model equals the complete vehicle mass. The height of the CG is therefore chosen equal to the total vehicle CG. u and v are now expressed in the total vehicle CG while they should be expressed in the platform CG according to earlier definitions. This deviation is accepted for this investigation. The base Newton Euler equations for translation and rotation are

$$\sum \vec{F}_{cog} = \dot{\vec{P}} \tag{E.4}$$

$$\sum \vec{M}_{cog} = \dot{\vec{H}} \tag{E.5}$$

where $\sum \vec{F}_{cog}$ and $\sum \vec{M}_{cog}$ the total force and torque accelerating the center

of gravity in body-fixed coordinate system, which are further defined as

$$\begin{aligned}
\vec{F}_{cog} &= \vec{F}_{rp} + m\vec{g} \\
&= \begin{bmatrix} \sum F_x & \sum F_y & mg \end{bmatrix} \underline{\vec{e}}^1 + m\vec{g} \\
&= \begin{bmatrix} \sum F_x & \sum F_y & 0 \end{bmatrix} \underline{\vec{e}}^1 \qquad \text{(E.6)} \\
\vec{M}_{cog} &= \vec{M}_{rp} - \vec{r} \times \vec{F}_{rp} \\
&= \begin{bmatrix} -k_\gamma \gamma - d_\gamma \dot{\gamma} & -k_\varphi \varphi - d_\varphi \dot{\varphi} & \sum M_z \end{bmatrix} \underline{\vec{e}}^1 \\
&\quad -h_2 \vec{e}_3^2 \times \begin{bmatrix} \sum F_x & \sum F_y & mg \end{bmatrix} \underline{\vec{e}}^1 \\
&\approx \begin{bmatrix} h_2 \sum F_y + mgh_2\varphi - k_\varphi \varphi - d_\varphi \dot{\varphi} \\ -h_2 \sum F_x + mgh_2\gamma - k_\gamma \gamma - d_\gamma \dot{\gamma} \\ -h_2 \varphi \sum F_x - h_2 \gamma \sum F_y + \sum M_z \end{bmatrix}^T \underline{\vec{e}}^1 \qquad \text{(E.7)}
\end{aligned}$$

Here, $\sum \vec{F}_{rp}$ is the total force in the roll pole, $\vec{r}$ the position vector from RP to COG and $\vec{g}$ the gravity vector. The time derivatives of the impulses are defined as

$$\begin{aligned}
\dot{\vec{P}} &= \frac{d}{dt}(m\dot{\vec{r}}_{cog}) \\
&= \frac{d}{dt}\left(m \begin{bmatrix} u & v & 0 \end{bmatrix} \underline{\vec{e}}^1\right) \\
&= m \begin{bmatrix} \dot{u} - v\dot{\Psi} & \dot{v} + u\dot{\Psi} & 0 \end{bmatrix} \underline{\vec{e}}^1 \qquad \text{(E.8)} \\
\dot{\vec{H}} &= \mathbf{J} \cdot \dot{\vec{\omega}} + \vec{\omega} \times (\mathbf{J} \cdot \vec{\omega}) \\
&\approx \begin{bmatrix} J_{xx}\ddot{\varphi} & J_{yy}\ddot{\gamma} & J_{zz}\ddot{\Psi} \end{bmatrix} \underline{\vec{e}}^1 \qquad \text{(E.9)}
\end{aligned}$$

Combining above four equations according to equations E.4 and E.5 will result in the next equations of motion.

$$
\begin{aligned}
m\dot{u} &= v\dot{\Psi} + \sum F_x \\
m\dot{v} &= -u\dot{\Psi} + \sum F_y \\
J_{xx}\ddot{\gamma} &= (-k_\varphi + mgh_2)\varphi - d_\varphi\dot{\varphi} + h_2 \sum F_y \\
J_{yy}\ddot{\varphi} &= (-k_\gamma + mgh_2)\gamma - d_\gamma\dot{\gamma} + h_2 \sum F_x \\
J_{zz}\ddot{\Psi} &= \sum M_z - h_2\varphi \sum F_x - h_2\gamma \sum F_y
\end{aligned}
\tag{E.10}
$$

Other interesting system outputs are the vertical wheel forces that define the maximum traction for each wheel. According to this model, the wheel load shifts will react instantly to the dynamics of equation E.10 to form static equilibrium.

$$\Delta F_{pitch} = \frac{-h_1 \sum F_x + k_\gamma\gamma + d_\gamma\dot{\gamma}}{4a} \tag{E.11}$$

$$\Delta F_{roll} = \frac{-h_1 \sum F_y - k_\varphi\varphi - d_\varphi\dot{\varphi}}{4s} \tag{E.12}$$

With ΔF_{pitch} the wheel load shift caused by pitch and ΔF_{roll} the wheel load shift caused by roll, where the forces per wheel are:

$$F_{tz1} = \frac{1}{4}mg + \Delta F_{pitch} + \Delta F_{roll} \tag{E.13}$$

$$F_{tz2} = \frac{1}{4}mg - \Delta F_{pitch} + \Delta F_{roll} \tag{E.14}$$

$$F_{tz3} = \frac{1}{4}mg - \Delta F_{pitch} - \Delta F_{roll} \tag{E.15}$$

$$F_{tz4} = \frac{1}{4}mg + \Delta F_{pitch} - \Delta F_{roll} \tag{E.16}$$

With F_{tzi}, the vertical force acting on wheel i.

This model is linearized around a constant forward velocity equilibrium and analyzed. The results will be discussed later in this appendix and compared with the other models.

Simmechanics model

Strong doubts exist about the validity of the pitch/roll model presented in the previous paragraph. The main doubts originate from the relative high mass of the corner modules and the influence of the in Z-direction infinitely stiff assumed tyres. A validation of this model is therefore necessary. A more detailed model would include the six degrees of freedom of the main platform and the translational degree of freedom of the four suspension systems which act under an angle. Analytically writing down the equations of motion of such a model would become an extensive work. It is chosen to model this system in Matlab's multibody software Simmechanics, which works within Simulink [14]. After modeling, by perturbation around equilibrium situation, linearized system matrices can be exported.

Comparison of models

Three models to describe the motion of the platform are now developed. The planar model, the analytical pitch/roll model and finally the Simmechanics model. The three models have increasing complexity. It must be determined how much the different models differ in responses. In this paragraph, the three models are compared by giving horizontal step force inputs at ground level. All models are symmetrical in pitch and roll direction. In figure E.4, the step response of pitch/roll angle is shown as a function of the time. In figure E.5, the response of vertical wheel load shifting is depicted. In the last figure E.6, the platform Center of Gravity acceleration is plotted with force step input at tyre level.

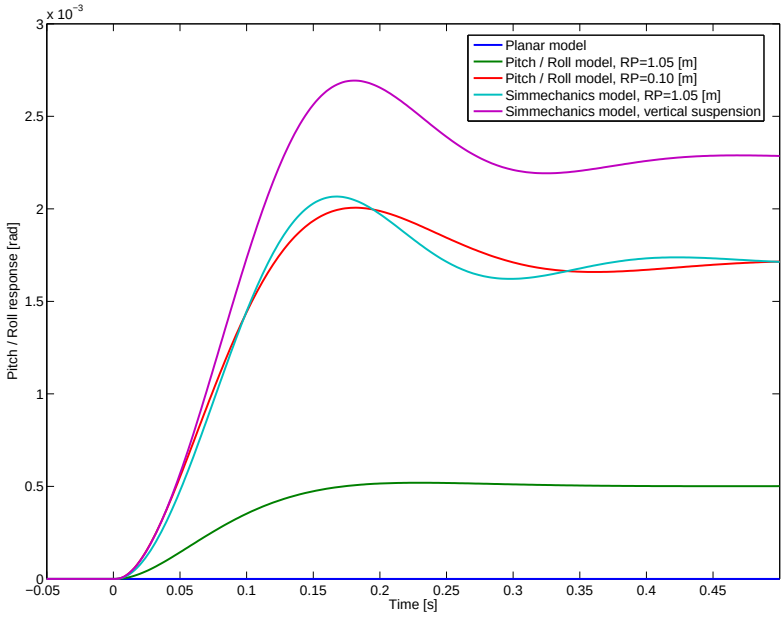

Figure E.4: Response of pitch/roll angle to 10,000 [N] step input

The planar model will give straightforward responses. No pitch or roll is possible. Acceleration acts instantaneously at the center of gravity and a direct load shift will occur. When the pitch/roll model and the Simmechanics models, with the same designed pitch/roll-pole height of 1.05 [m] are compared, large differences in responses are found. The Simmechanics model shows much larger responses in pitch and roll than the optimistic pitch/roll model. The pitch/roll pole of the pitch/roll model is lowered to 0.10 [m] where about the same magnitude in responses are obtained. From this survey, it seems like the effect of the height of the theoretic roll/pitch pole is overestimated. The question arises how much the total effect is from using anti-pitch/roll in the suspension instead of using a vertical suspension. Therefore, the Simmechanics model is also executed for a vertical suspension system and depicted in the above figures. Placing the suspension under an angle indeed shows effect, however, with a static pitch/roll analysis, this effect is highly overestimated.

The different models show different responses in COG acceleration. All responses consist of a step and the multibody model shows an additional transient part. In this survey, a step in force is applied at the corner modules at ground level independently of model responses. In reality, this force

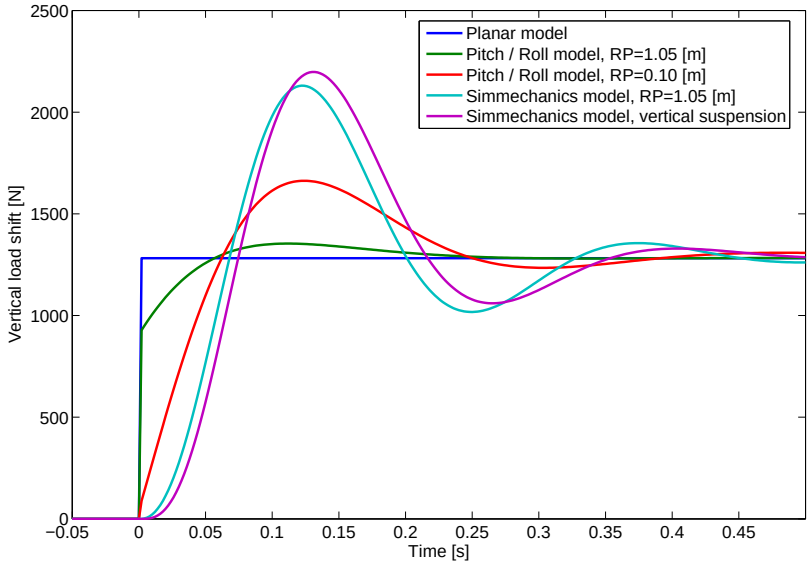

Figure E.5: Response vertical wheel force to 10,000 [N] step input

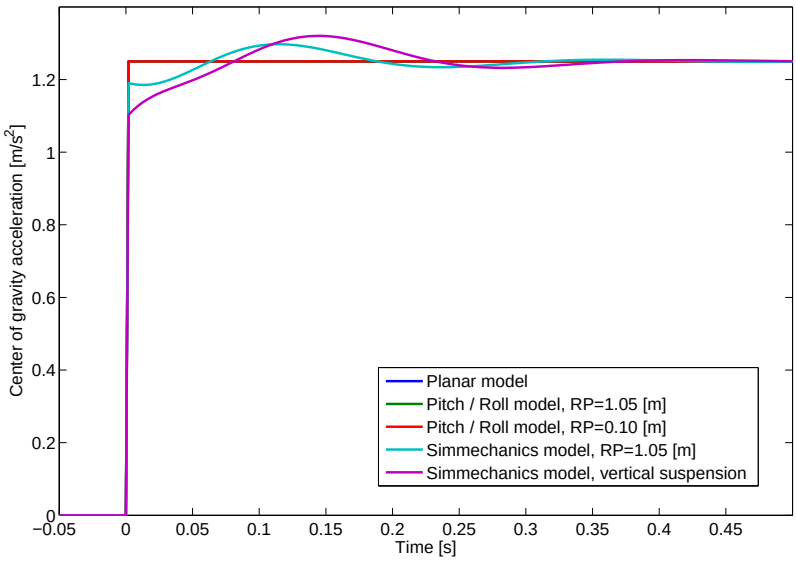

Figure E.6: Response Center of Gravity acceleration to 10,000 [N] step input

is generated by the tyres. The tyres produce a force based on velocity differences between the vehicle and the ground. When the vehicle starts rolling, this influences corner module speed which again influences corner module force. The model output starts interacting with the model input through the tyres. In conclusion, a more complicated model is obtained. In the next section, the tyres will be investigated.

Appendix F

Tyre models

The tyre is a crucial part of the ATV. The total ATV dynamical behavior will be strongly influenced by the tyres [3]. For that reason, this appendix will describe different tyre models. All tyre models explained in this chapter are discussed in more detail in reference [15].

First, some general relations will be explained. In general, it can be said that tyre forces are caused by slip between the tyre contact patch and the ground in longitudinal direction κ and lateral direction α. Furthermore, the tyre force is dependent on the vertical load F_z and there is also a effect present of the camber angle γ of the wheel.

$$F_{tx} = F_{tx}(\kappa, \alpha, F_z, \gamma) \tag{F.1}$$
$$F_{ty} = F_{ty}(\kappa, \alpha, F_z, \gamma) \tag{F.2}$$
$$M_{tz} = M_{tz}(\kappa, \alpha, F_z, \gamma) \tag{F.3}$$

Slip is defined by the velocity difference between the contact patch and the ground divided by the total forward velocity,

$$\kappa = -\frac{V_x - r_e\omega}{V_x} = -\frac{\omega_0 - \omega}{\omega_0} \tag{F.4}$$
$$\tan\alpha = -\frac{V_{sy}}{V_x} \tag{F.5}$$

with V_x the longitudinal velocity of the wheel, V_{sy} the lateral slip velocity of the wheel, ω the rotational velocity of the wheel, r_e the effective rolling

radius and ω_0, the omega where no longitudinal slip would occur. In this thesis, the effective rolling radius r_e is defined as

$$r_e = \frac{V_x}{\omega_0} \tag{F.6}$$

And a similar slip velocity in x-direction V_{sx} can be defined as for the slip velocity as it exists for the y-direction V_{sy},

$$V_{sx} = V_x - r_e\omega \tag{F.7}$$

The signs of the forward and side slip are defined in such a way that a positive slip will create a positive force. During braking, the slip becomes negative, while during driving, the slip becomes positive.

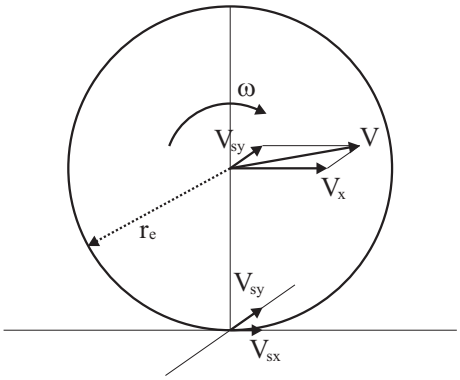

Figure F.1: Definition of speeds and slip

Steady state tyre behavior

In this section, the steady state tyre models will be discussed. Reacting forces because of slip are analyzed and dynamic influences from carcass stiffness and inertia are omitted. This will be included later in this appendix.

The different models will differ in complexity and can be analytical or empirical. Analytical models will give some understanding as to why certain responses can be expected while empirical models will match better with measurement data. Firstly, the simplest linear tyre will be discussed followed by the analytical brush model and finally the empirical magic formula.

Linear tyre

The steady state linear tyre model is straightforward. Longitudinal and lateral tyre forces are linear dependent on slip velocities.

$$F_{tx} = C_{f\kappa}\kappa \tag{F.8}$$
$$F_{ty} = C_{f\alpha}\alpha \tag{F.9}$$

Generally, the two slip stiffnesses $C_{f\kappa}$ and $C_{f\alpha}$ are dependent on the vertical load. A higher load will increase the the values of these parameters. The vertical load will be assumed constant when this model is used in this paper however. The values of $C_{f\kappa}$ and $C_{f\alpha}$ for the ATV truck tyre at a nominal load F_{zN} of 19,620 [N] can be found in table 2.2.

Brush model

The brush model is a more sophisticated model based on a physical insight in tyres. The tyre is considered a disk with a single row of bristles that are compliant in forward and lateral direction like a brush. This is depicted in figure F.2.

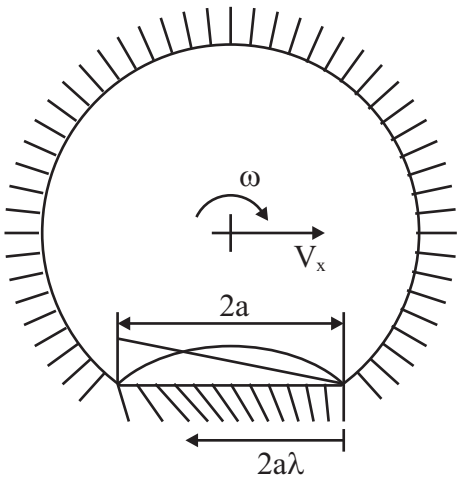

Figure F.2: Brush model principle

First of all, all the bristles are undeformed when they are not in contact with the ground. A part of the tyre is in contact with the ground and assumed to be flat. The length of the contact region $2a$ is dependent on the

vertical force F_z. Within this region $2a$, a parabolic pressure distribution is assumed. At the moment the bristles first enter the contact region $2a$, they are positioned vertical. However, while moving forward, there is a speed difference/slip present that makes the bristles deflect. Since the bristles have a certain stiffness, the bristle will generate a tyre force. When the slip becomes large, the bristles will deform too much and generate a higher force than could physically be expected. Therefore, a transition point is present where the bristles transform from adhesion to sliding. The position of this transition point is located at $2a\lambda$ and is dependent on the tyre slip κ and α. The self aligning moment M_z can be determined by the force distribution in the contact region.

The bristle model creates analytical equations for the tyre forces F_{tx}, F_{ty} and self aligning moment M_{tz} based on a physical model. The amount of sliding is conveniently determined by the adhesion/sliding parameter λ. For very large slip ratios, no decrease in tyre force is generated as can be seen in real tyres. A more complicated model is needed if the stiffness in x- and y-direction are chosen different. The self aligning moment is strongly underestimated and no good dependency of vertical load is present.

In the next subsection, the more accurate measurement data based semi-empirical magic formula tyre model is discussed. The obtained knowledge from the brush model is useful for understanding responses.

Magic formula

The magic formula based tyre model is a widely used semi-empirical tyre model. This model was developed in the mid eighties and extended ever since. Some different versions are available [15]. The general form of the magic formula which is based on a sine and arctan function is formulated below.

$$y = D\sin[C\arctan\{Bx - E(Bx - \arctan(Bx))\}]; \tag{F.10}$$

where x is the input, y the output and A,B,C, D and E shape factors. The input x can for example, be a slip while the output y can typically represent a tyre force. The shape factors B, C, D and E define the shape of the curvature. D determines the peak value, C determines the limit value for $x \to \infty$, $B \cdot C \cdot D$ determines the slope at the origin and E determines the location of the peak. The curve can also get a horizontal and vertical offset by using shift-factors in the input and output. The magic formula curve of the 315-80-R22 truck tyre is plotted in figure F.3.

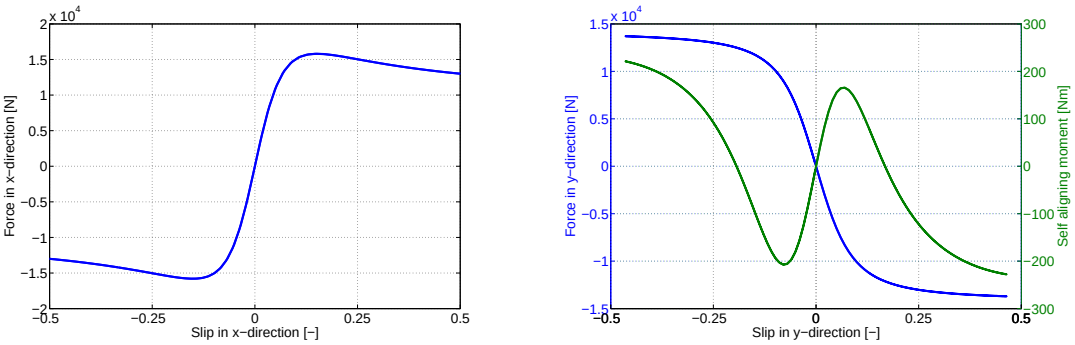

Figure F.3: Magic formula curves for truck tyre with $F_z = 19,620$ [N]

The shape parameters of the curve depend on a number of variables. Most of them will change with varying vertical force. When, as well slip in x-direction, as slip in y-direction are present, combined slip takes place, where additional equations are needed for. Camber affects and self aligning torque are also being seen in real tyres. This makes that some magic formula tyre models get very extended with a huge number of parameters.

A more comprehensible approach of the magic formula is the similarity method. This method is based on approximately similar shaped curves for pure slip curves at different conditions. The curve can be scaled in x- and y-direction, which equals input and output scaling. Additional horizontal and vertical shifts can be added. For combined slip conditions, an approach similar to that of the brush model is followed. The total slip is quadratically determined out the longitudinal and lateral slip and used in the independent longitudinal and lateral tyre formulas. The longitudinal force is the portion of the longitudinal slip of the total slip times the resulting force form the longitudinal magic formula. The lateral force is the portion of the lateral slip of the total slip times the resulting force form the lateral magic formula. The similarity method uses considerably less parameters and gives a good understanding of tyre behavior. The representation of reality will be less than with the full magic formula however.

If the most realistic possible tyre behavior is persuaded, commercial software is advised. For this research the Delft-Tyre package, developed by Delft University of Technology and TNO is used for validation [6].

Transient tyre behavior

In the last subsection, steady state tyre models were discussed. Different models are presented which will represent tyre behavior in different levels of accuracy. As discussed, the dynamics of tyres will play an important role in final ATV responses. Therefore, different ways to handle the dynamics of the tyre will be treated in this section.

Linear model

In the linear transient tyre model, the carcass stiffness is represented by a linear spring. This spring connects the wheel rim with the contact patch of the tyre. The contact patch behaves as a velocity and normal force dependent damper as described in the first part of this appendix. The carcass deflections in x and y direction are named u_t and v_t as depicted in figure F.4.

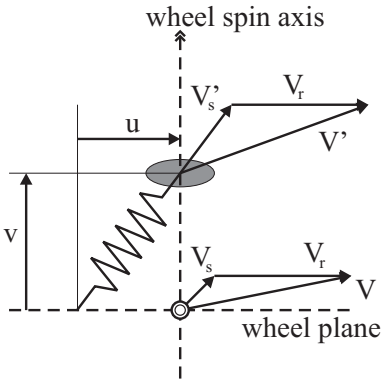

Figure F.4: Deflection of the contact point

The longitudinal properties are described with the following equations. The tyre deflection, slip velocities and slips in the contact patch are denoted as

$$\dot{u_t} = {V_{sx}}' - V_{sx} \tag{F.11}$$

$$\kappa' = -\frac{{V_{sx}}'}{|V_x|} \tag{F.12}$$

with u_t deflection of the tyre in x-direction, κ' slip of contact patch and ${V_{sx}}'$ the longitudinal slip of the contact patch. To form equilibrium of forces in the contact patch, the force caused by slip has to equal the force of the carcass stiffness.

$$F_{tx} = C_{fx} u_t \tag{F.13}$$

$$F_{tx} = C_{f\kappa} \kappa' \tag{F.14}$$

Now, equate equations F.13 and F.14, replace κ' with equation F.12 and ${V_{sx}}'$ with equation F.11. The following result for longitudinal deflection is obtained.

$$\dot{u_t} + \frac{C_{fx}}{C_{f\kappa}} |V_x| u_t = -V_{sx} \tag{F.15}$$

If u is again replaced with equation F.13, and the following result in tyre force F_{tx} is obtained

$$\frac{1}{|V_x|} \sigma_\kappa \dot{F_{tx}} + F_{tx} = -C_{f\kappa} \frac{V_{sx}}{|V_x|} \tag{F.16}$$

where the relaxation length σ_κ is

$$\sigma_\kappa = \frac{C_{f\kappa}}{C_{fx}} \tag{F.17}$$

For practical use, equation F.16 should be multiplied with $|V_x|$ on both sides to avoid singularities around standstill. A similar derivation as for longitudinal direction can be done for lateral slip and forces. With adding some extensions, the method can even succeed in giving approximations for lateral forces caused by camber and self aligning moments.

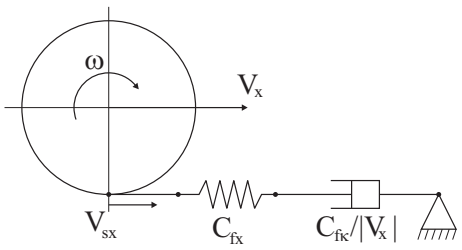

Figure F.5: Spring-damper representation of tyre

Figure F.5 gives a visualization of the obtained differential equation. At standstill, the tyre will behave like a spring, while at higher longitudinal speeds, the damper behavior becomes more significant.

Since the ATV is driving at relatively slow velocities, this is an indicator the carcass stiffness might indeed play a significant role. The parameters of this model for the ATV truck tyre are listed in table 2.2.

Non-linear model

The semi-non-linear tyre model uses equation F.15 to determine κ'. Similar expressions are available for α' and γ'. These variables are directly used in the non-linear Magic Formula. Zero speed simulations are possible. Because of the integrating action of equation F.15, at low speeds, the possibility of getting physically impossible carcass deflections exists. This needs to be limited. In the extreme situation of wheel lock, the theoretical carcass deflection u_t becomes as large as the relaxation length σ_κ. Further is shown that in real tyres, at a high slip rate, responses become faster. This model can represent tyre properties up to 8 Hz and wavelengths larger than the tyre circumference. The commercial version of this model is called MF-Tyre and available in the Delft-Tyre package [6]. This model will be used for validation purposes.

In the fully-non-linear tyre model, the relaxation length decreases with higher levels of slip.

Enhanced non-linear model

In the latter models, the contact patch slip properties and the carcass compliance is separated by the relaxation length. Another way is explicitly modeling the both. This is done by adding a small mass to the contact patch. A simple physically logical model is obtained. A disadvantage however is that the small mass may lead to a system with high eigenfrequencies that causes a low computational velocity. Figure F.6 that shows the contact patch and carcass deflections is included to clarify the signs of different quantities.

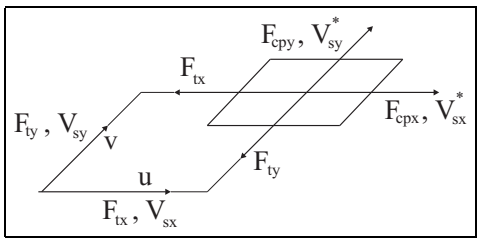

Figure F.6: Sign definitions for enhanced non-linear model

The equations for the enhanced non-linear model are

$$m_c \dot{V}'_{sx} = -k_{cx}\dot{u}_t - c_{cx}u_t + F_{cpx}(\kappa', \alpha', F_z, \gamma') \tag{F.18}$$

with F_{cpx}, the force in x-direction generated by the tyre contact patch and V_{sx} as input

$$\dot{u}_t = V_{sx}{}' - V_{sx} \tag{F.19}$$

and the force at the rim as output.

$$F_{tx} = k_{cx}\dot{u} + c_{cx}u \tag{F.20}$$

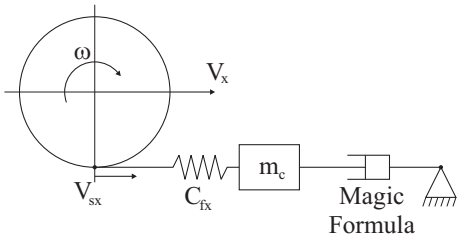

Figure F.7: Spring-damper representation of tyre

SWIFT model

SWIFT model stands for Short Wavelength Intermediate Frequency Tyre model and is designed by the Delft university of technology and TNO. This model simulates the carcass and contact patch as different inertias and gives good dynamical responses up to frequencies of 60-100 Hz. This model is advanced and requires many parameters. The commercial version of this model is called SWIFT-Tyre and available in the Delft-Tyre software [6]. This model will not be used because the dynamical range is exceeding the region of interest of this research.

Appendix G

Planar equations of motion

This appendix contains the complete equations of motions derived in subsection 4.2 and executed with the Matlab symbolic toolbox.

```
f1=
v*PsiP+1/m*(Cfx*ut1*cos(delta1)-Cfy*vt1*sin(delta1)+Cfx*ut2*cos(delta2)-Cfy*vt2*sin(delta2)...
+Cfx*ut3*cos(delta3)-Cfy*vt3*sin(delta3)+Cfx*ut4*cos(delta4)-Cfy*vt4*sin(delta4));
f2=
-u*PsiP+1/m*(Cfx*ut1*sin(delta1)+Cfy*vt1*cos(delta1)+Cfx*ut2*sin(delta2)+Cfy*vt2*cos(delta2)...
+Cfx*ut3*sin(delta3)+Cfy*vt3*cos(delta3)+Cfx*ut4*sin(delta4)+Cfy*vt4*cos(delta4));
f3=
s/J*(-Cfx*ut1*cos(delta1)+Cfy*vt1*sin(delta1)-Cfx*ut2*cos(delta2)+Cfy*vt2*sin(delta2)...
+Cfx*ut3*cos(delta3)-Cfy*vt3*sin(delta3)+Cfx*ut4*cos(delta4)-Cfy*vt4*sin(delta4))...
+a/J*(Cfx*ut1*sin(delta1)+Cfy*vt1*cos(delta1)-Cfx*ut2*sin(delta2)-Cfy*vt2*cos(delta2)...
-Cfx*ut3*sin(delta3)-Cfy*vt3*cos(delta3)+Cfx*ut4*sin(delta4)+Cfy*vt4*cos(delta4));
f4=
-Cfx/Cfk*abs((u-s*PsiP)*cos(delta1)+(v+a*PsiP)*sin(delta1))*ut1...
-(u-s*PsiP)*cos(delta1)-(v+a*PsiP)*sin(delta1)+omega1*Re;
f5=
(omegaref1-omega1)*Cqc/Jw-Re*Cfx*ut1/Jw;
f6=
-Cfy/Cfa*abs((u-s*PsiP)*cos(delta1)+(v+a*PsiP)*sin(delta1))*vt1...
+(u-s*PsiP)*sin(delta1)-(v+a*PsiP)*cos(delta1);
f7=
1/tau_hydr*(deltaref1-delta1);
f8=
-Cfx/Cfk*abs((u-s*PsiP)*cos(delta2)+(v-a*PsiP)*sin(delta2))*ut2...
-(u-s*PsiP)*cos(delta2)-(v-a*PsiP)*sin(delta2)+omega2*Re;
f9=
(omegaref2-omega2)*Cqc/Jw-Re*Cfx*ut2/Jw;
f10=
-Cfy/Cfa*abs((u-s*PsiP)*cos(delta2)+(v-a*PsiP)*sin(delta2))*vt2...
+(u-s*PsiP)*sin(delta2)-(v-a*PsiP)*cos(delta2);
f11=
1/tau_hydr*(deltaref2-delta2);
f12=
-Cfx/Cfk*abs((u+s*PsiP)*cos(delta3)+(v-a*PsiP)*sin(delta3))*ut3...
-(u+s*PsiP)*cos(delta3)-(v-a*PsiP)*sin(delta3)+omega3*Re;
f13=
(omegaref3-omega3)*Cqc/Jw-Re*Cfx*ut3/Jw;
f14=
-Cfy/Cfa*abs((u+s*PsiP)*cos(delta3)+(v-a*PsiP)*sin(delta3))*vt3...
+(u+s*PsiP)*sin(delta3)-(v-a*PsiP)*cos(delta3);
f15=
1/tau_hydr*(deltaref3-delta3);
f16=
```

```
-Cfx/Cfk*abs((u+s*PsiP)*cos(delta4)+(v+a*PsiP)*sin(delta4))*ut4...
-(u+s*PsiP)*cos(delta4)-(v+a*PsiP)*sin(delta4)+omega4*Re;
f17=
(omegaref4-omega4)*Cqc/Jw-Re*Cfx*ut4/Jw;
f18=
-Cfy/Cfa*abs((u+s*PsiP)*cos(delta4)+(v+a*PsiP)*sin(delta4))*vt4...
+(u+s*PsiP)*sin(delta4)-(v+a*PsiP)*cos(delta4);
f19=
1/tau_hydr*(deltaref4-delta4);
```

Appendix H

Quadratic minimization

The optimization procedure of allocation strategy 2 of section 5.2 will be handled in this appendix. For a convenient notation, the minimization parameters are placed in the vector $\underline{x}$.

$$\underline{x} = \begin{bmatrix} F_{cmx1} & F_{cmy1} & F_{cmx2} & F_{cmy2} & F_{cmx3} & F_{cmy3} & F_{cmx4} & F_{cmy4} \end{bmatrix}^T \tag{H.1}$$

The formal natation of a minimization problem like the one of section 5.2 is:

$$\begin{aligned} \min_{\underline{x}} \quad & f(\underline{x}) \\ & \textit{subject to } \underline{h}(\underline{x}) = \underline{0} \end{aligned} \tag{H.2}$$

Where for this specific case, the minimization function f is defined as

$$f(\underline{x}) = \frac{F_{cmx1}^2}{F_{tz1}^2} + \frac{F_{cmy1}^2}{F_{tz1}^2} + \frac{F_{cmx2}^2}{F_{tz2}^2} + \frac{F_{cmy2}^2}{F_{tz2}^2} + \frac{F_{cmx3}^2}{F_{tz3}^2} + \frac{F_{cmy3}^2}{F_{tz3}^2} + \frac{F_{cmx4}^2}{F_{tz4}^2} + \frac{F_{cmy4}^2}{F_{tz4}^2} \tag{H.3}$$

and the constraints $\underline{h}$ are

$$\underline{h}(\underline{x}) = \begin{bmatrix} F_{cmx1} + F_{cmx2} + F_{cmx3} + F_{cmx4} - \sum F_x \\ F_{cmy1} + F_{cmy2} + F_{cmy3} + F_{cmy4} - \sum F_y \\ 2\sqrt{2}(-F_{cmx1} + F_{cmy1} - F_{cmx2} - F_{cmy2}) + ... \\ \qquad 2\sqrt{2}(+F_{cmx3} - F_{cmy3} + F_{cmx4} + F_{cmy4}) - \sum T_z \end{bmatrix} \tag{H.4}$$

Quadratic programming without constraints

For didactically reasons, first the minimization procedure without constraints will be treated. Later on, the constraints will be added again.

The function $f(\underline{x})$ around a certain value of $\underline{x}$ can be described in a serie of tailor expansions:

$$\begin{array}{l} f(\underline{x}+\Delta\underline{x}) = \\ f(\underline{x}) + \nabla f \cdot \Delta\underline{x} + \frac{1}{2}\nabla^2 f \cdot \underline{x}^2 + ... = \\ f(\underline{x}) + g(\underline{x}) \cdot \Delta\underline{x} + \frac{1}{2}\Delta\underline{x}^T \cdot H(\underline{x}) \cdot \Delta\underline{x} + ... \end{array} \tag{H.5}$$

Close enough to the value $\underline{x}$, $\Delta\underline{x}$ will become small and the higher order terms multiplied with $\Delta\underline{x}$ to a certain power will become negligible. Only the first two derivatives are taken along. In stepwise notation this is written as:

$$f_{k+1} = f_k + g_k \delta\underline{x}_k + \frac{1}{2}\delta\underline{x}_k^T H_k \delta\underline{x}_k \tag{H.6}$$

The derivative of $f(\underline{x})$ can also be approached by a series of taylor expansions.

$$\nabla f(\underline{x}+\Delta\underline{x}) = \nabla f(\underline{x}) + \nabla^2 f \cdot \Delta\underline{x} + ... = g(\underline{x}) + H(\underline{x})\Delta\underline{x} + ... \tag{H.7}$$

$$\nabla f_{k+1}^T = g_k + H_k \delta\underline{x}_k \tag{H.8}$$

At the optimum, the derivative of $f(\underline{x})$ is zero

$$g_k + H_k \delta\underline{x}_k = 0 \tag{H.9}$$

This can be found by making an iterative step s according to Newton's method [18].

$$\underline{s} = H_k^{-1}\underline{g}_k \tag{H.10}$$

$$\underline{x}_{k+1} = \underline{x}_k - H_k^{-1}\underline{g}_k \tag{H.11}$$

Since quadratic functions have a constant Hessian or second derivative and no higher order terms, the minimizer (value of $\underline{x}$ at which $f(\underline{x})$ is minimal) is found in one step.

Quadratic programming with linear equality constraints

A minimization procedure for quadratic functions has been found. Now, the constraints will be added.

For this purpose, the following lagrangian will be defined:

$$L = f + \underline{\lambda}^T \underline{h} \tag{H.12}$$

With the Karish-Kuhn-Tucker (KKT) conditions:

$$\nabla L = \nabla f + \underline{\lambda}^T \nabla \underline{h} = \underline{0}^T \tag{H.13}$$

$$\underline{h} = \underline{0} \tag{H.14}$$

$$\underline{\lambda} \neq \underline{0} \tag{H.15}$$

The analogy with the minimization of the original function $f(\underline{x})$ is clear. Now, the minimizer is found at the moment the gradient of $L(\underline{x}, \underline{\lambda})$ is zero. The problem is changed from minimizing the function $\underline{x}$ to minimizing $L(\underline{x}, \underline{\lambda})$.

In the original system, the gradient of the function $f(\underline{x})$ has to be zero at the minimizer. This does not longer apply for the constrained problem. The constraints will move the minimum to another position and therefore create a gradient of the function $f(\underline{x})$ at that position. The KKT conditions can be interpreted in such a way that the constraints perform such a gradient that the summed gradient of the original function $f(\underline{x})$ and $\underline{\lambda}$ times the constraints $\underline{h}(\underline{x})$ are zero again.

The constraints stated in this specific minimization problem are well posed and create a quadratic lagrangian. With the use of Newton, this problem can be solved in one step [18] with the next equation.

$$\begin{bmatrix} W_0 & A_0^T \\ A_0 & 0 \end{bmatrix} \begin{bmatrix} \underline{x}_* \\ \underline{\lambda}_* \end{bmatrix} = \begin{bmatrix} -\nabla f_0^T \\ -\underline{h}_0 \end{bmatrix} \tag{H.16}$$

with

$$A_0 = \nabla \underline{h}(\underline{0}) \tag{H.17}$$

$$W_0 = \nabla^2 f(\underline{0}) + 0 \tag{H.18}$$

Appendix I

Controller design results

Chapter 7 explains the design of the controller. A number of figures are shown in this chapter to demonstrate the design procedure. With an extensive design such as with an 8×8 controller, many more results need to be checked. To keep chapter 7 orderly some of these figures are presented in this appendix.

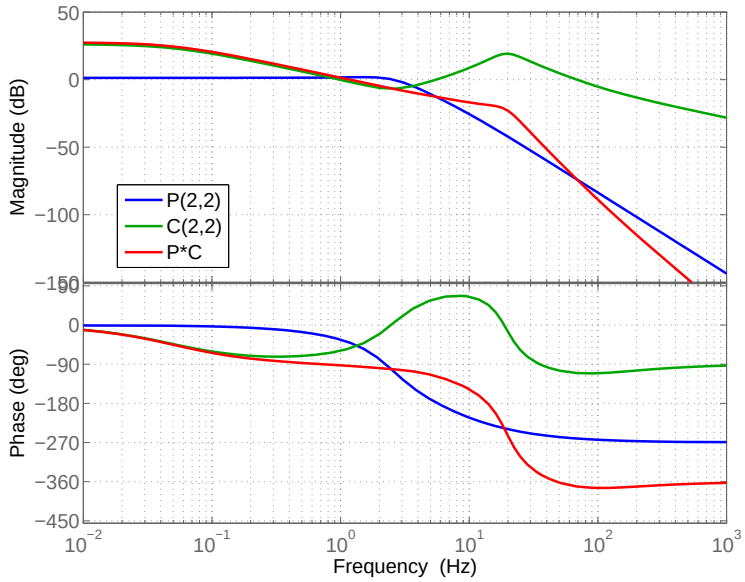

Figure I.1: Lateral plant and controller

Figure I.1 shows the bode diagram of the (2,2) element of the plant, the

controller and the multiplication of both. For an SISO system, these figures would tell something about open loop behavior, stability margins and bandwidth. For this MIMO system, this theory is not valid. However, because of the pure lateral movement, symmetry in the vehicle exists. Imagine the plant line being 12 dB raised (factor 4) because of the four actuators working simultaneous.

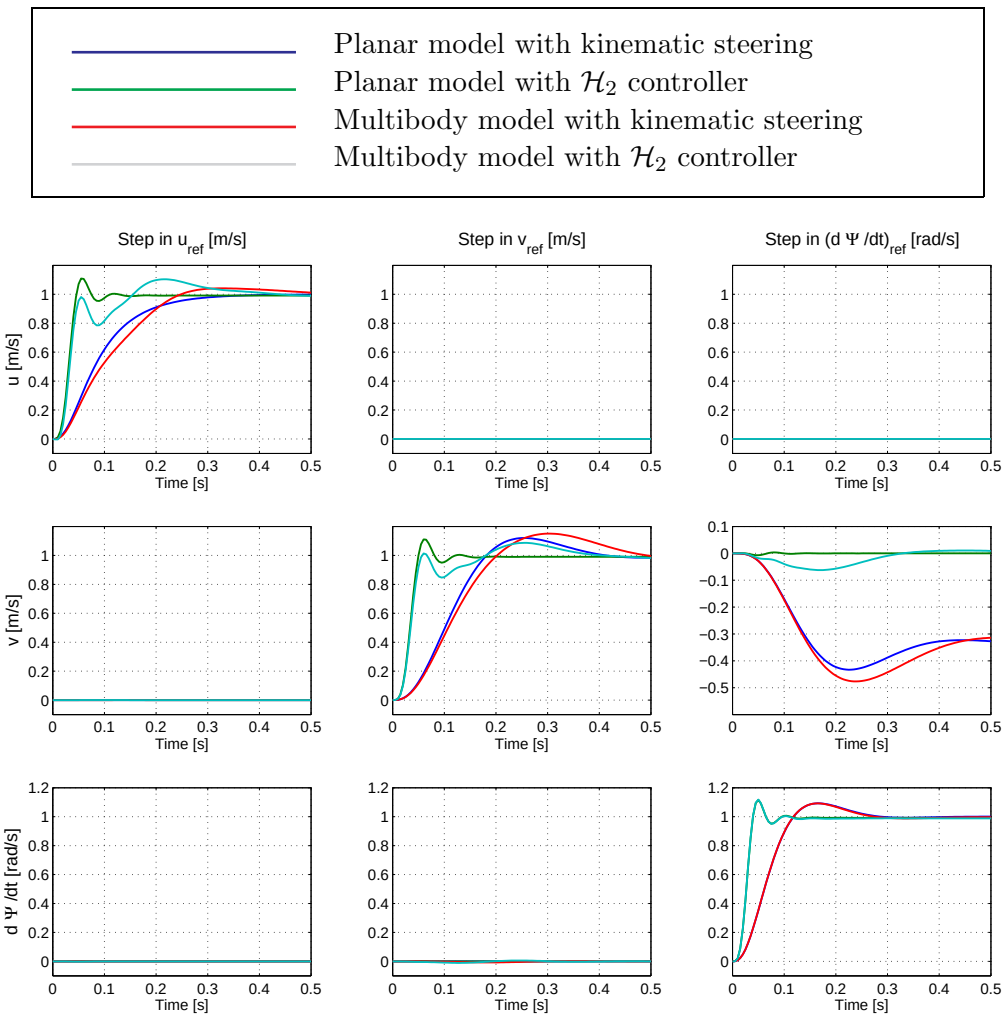

Figure I.2: Step responses of kinematic steering HR and $\mathcal{H}_2$ control $\frac{PC}{I+PC}$

Except for a frequency domain analysis, the time domain step responses always do help understanding the controlled behavior. The both the planar as the multibody model linearized around a forward velocity of 5 m/s are used. To show the difference between the uncontrolled system, kinematic

steering is also used as a reference for wheel speeds and steering angles.

Figure I.3 shows a step in the reference yaw acceleration. At five seconds, the ATV has to accelerate with $5\sqrt{2}/8\ rad/s^2$. In the case of kinematic this would result in an inner steering angle of 45^o in one second. The acceleration lasts for one second. By giving this step input, two properties can be evaluated. First, how strong the controller reacts on step accelerations, and secondly how much performance is lost in the case of maximum steering in a complete other working point than the straight line driving on which the controller is designed. The first figure shows the reference, the second and the third figures show the controller outputs.

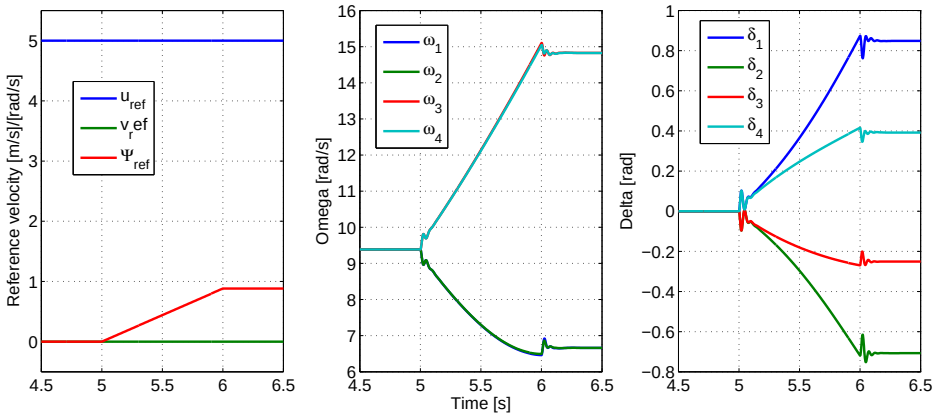

Figure I.3: Time responses for step in reference yaw acceleration

The actuators clearly show a strong differentiating action when the step inputs is given. This is necessary for a fast response. The maximum allowable driving torque is reached when the wheel speed error is 1 rad/s. With almost a step in the reference wheel speed of only 1/2 rad/s, the driving motors will not get saturated. In close-up, the steering angle reference accelerates approximately 5 rad/s^2 during the first 0.02 seconds. This is a very high acceleration during a short period of time. A step as reference is not a good choice because the system will not be able to track this signal under any circumstances. Higher order references are preferred such as constant jerk trajectory.

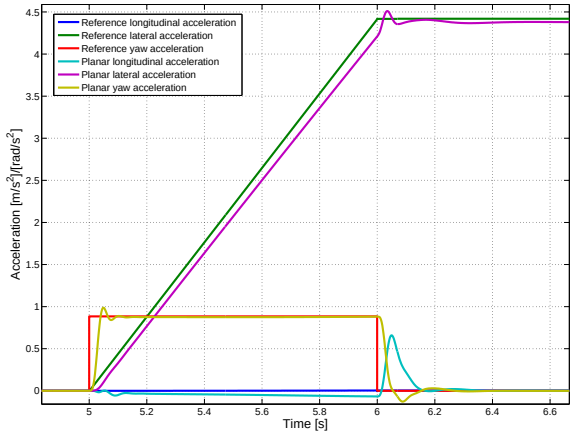

Figure I.4: Acceleration response for step in reference yaw acceleration

Clear disturbances due to non-linearitys during cornering can be observed in figure I.4. The chosen trajectory is an extreme situation and therefore concludes that this response is acceptable. Figure I.4 also very clearly shows the present time delay.